# Nanomaterial for High-Density Magnetic Data Storage[1]

## S. P. Gubin*, Y. I. Spichkin*, G. Yu. Yurkov*, and A. M. Tishin**

*\* Kurnakov Institute of General and Inorganic Chemistry, Russian Academy of Sciences,
Leninskii pr. 31, Moscow, 119991 Russia*
*\*\* Moscow State University, Vorob'evy gory, Moscow, 119899 Russia*

## 1. INTRODUCTION

The interdisciplinary field of mesoscopic and nanoscale systems is important for fundamental physics, as well as for some new technologies. Nanometer-sized structures are an intermediate form of matter, which fills the gap between atoms/molecules and bulk materials. These types of structures frequently exhibit exotic physical and chemical properties differing from those observed in bulk three-dimensional materials.

Advanced heterostructures with nanosized components have been the subject of much investigation in recent years [1–3]. The real advance in this direction is the development of new functional materials and the use of novel principles of device functioning. The tendency in the development of high technologies is toward direct physical and interdisciplinary investigations in the field of mesoscopic and nanoscale systems. One way to progress in the field of high-density data storage systems is to utilize magnetic nanoparticles (magnetic particles with sizes on the nanometer scale). In this context, systems of magnetic nanoparticles embedded in various matrices are particularly promising.

Generally, the electrical and magnetic behavior of nanostructured systems is governed by both the intrinsic properties of the nanostructures and their interactions with the matrix. Thus, the magnetic behavior of the system can be controlled by the size, shape, chemical composition, and structure of the nanoparticles and/or by the nature of the matrix in which they are embedded. However, the preparation of stable magnetic nanoscale materials that contain uniformly distributed nanoparticles (in a specified range of sizes of nanoparticles with a narrow size distribution) using conventional techniques is rather difficult. The fabrication and future utilization of such types of nanosized systems require using novel technological processes.

The areal data density on magnetic media, especially hard disk memory, has increased at an astonishing rate over the last three decades (30% per year for 1970–1990, 60% per year since 1990, and up to 100% per year in recent years). Extrapolating the 60–100% growth rate leads to bit sizes which clearly cannot be achieved using current technology [4]. In recent years, increasing the data storage density has meant decreasing the number of magnetic grains needed to store a bit of data from a thousand down to a few hundred and also decreasing the grain size. Today, the highest density hard disk drives store up to 120 billion bits (120 Gb) per square inch of the disk surface. As the bit density increases, all components of the system—the media, read head, write head, tracking system, detection and error correction electronics, etc.—become more difficult to design and construct. The fabrication of appropriate magnetic media is one of the most serious problems and is the major objective of our investigations.

All magnetic data recording systems are currently based on the media, which are comprised of a thin sheet containing small, single-domain, magnetically decoupled particles, which switch independently [4]. The granularity of the medium produces noise, which becomes unacceptable at small bit sizes. The media noise is now the primary factor that limits ultra-high-density magnetic recording systems. Reducing the grain size, which reduces noise, is a challenge, because there is a critical size of the thermal instability of magnetization [4]. To solve this problem, the particles should have a strong magnetic anisotropy. The single-domain status of the particles is important, because it prevents the undesirable magnetization reversal through domain wall motion.

All current commercial disk drive systems (excluding optical memories) operate using continuous granular media magnetized in-plane, called longitudinal recording. The magnetic recording industry has an enormous investment in longitudinal recording technology and is understandably very reluctant to move to an alternate technology. A number of disk drive companies commissioned a study, managed by the National Storage Industry Consortium (NSIC), to determine the limit on conventional longitudinal magnetic recording. The study group concluded that the extension of continuous longitudinal recording to 100 Gbit/in$^2$ was not impossible. The study concluded that a grain diameter of 8 nm, with an appropriately adjusted anisotropy field (6000 Oe), would meet both the thermal stability and the signal/noise requirements [4]. Media with an average grain size of 8 nm should not be extraordinarily hard to generate, but the model imposes another, very difficult to achieve requirement on the grain size, namely, that the grains should be monodisperse. In sum-

---

[1] This article was submitted by the authors in English.

mary, it would not be accurate to say that 100 Gbit/in$^2$ can never be achieved with longitudinal continuous media, but that to achieve such a density a new technology, leading to small (less than 10%) dispersal in grain size, needs to be invented.

A perpendicular continuous granular material exhibits a higher thermal stability than longitudinal media, because the demagnetizing fields are stabilizing rather than destabilizing and the grains can be larger since they can be columns, having small in-plane dimensions, which is important for short bit lengths, while achieving larger volumes due to a greater media thickness. Perpendicular magnetic recording has been extensively studied, but no commercially available systems presently use perpendicular recording. It seems problematic that the industry will abandon its enormous investment in longitudinal magnetic recording technology and plunge into unknown problems associated with perpendicular recording [4]. Perpendicular continuous media might well achieve 100 Gbit/in$^2$ [4], but very probably would need patterned media to solve the size dispersion problem. At the same time, as is currently believed, the patterned media cannot run into physical limitations until beyond 1 Tbit/in$^2$.

Patterned media, where each bit is a single domain, make it possible to substantially increase the achievable bit density. In theory at least, a bit having only one "grain" may be thermally stable down to a bit volume $n$ times smaller than that of the bit containing $n$ grains. Patterned media come in several varieties: perpendicularly magnetized rods, thin film islands magnetized either longitudinally or perpendicularly, etc. There is also a variety that resembles conventional granular media, with many grains per bit, but with the grains generated as a regular array of identical grains, which solves the grain size dispersion problem.

Recently, three-dimensional superlattices consisting of monodisperse iron–platinum nanoparticles with sizes tunable from 3 to 10 nm were synthesized at the IBM T.J. Watson Research Center (Yorktown Heights, NY) [5]. First, the monodisperse FePt colloid was obtained, using oleic acid and oleyl amine as stabilizers, through reduction of platinum acetylacetonate by a diol and high-temperature decomposition of iron pentacarbonyl Fe(CO)$_5$ in solution. The composition of the particles was adjusted by controlling the molar ratio of iron pentacarbonyl to platinum salt. Then, the particles were isolated, purified by centrifugation after the addition of a flocculent (ethanol), redispersed in a nonpolar solvent, and spread on a substrate, followed by carrier solvent evaporation. This procedure resulted in the nanoparticles self-assembling into three-dimensional superlattices on the substrate surface with a thickness up to 200 nm. In these structures, nanoparticles were maintained by oleic acid and oleyl amine capping groups. For example, for 6-nm Fe$_{50}$Pt$_{50}$ nanoparticles, a hexagonal close-packed three-dimensional array with a nearest neighbor spacing of about 4 nm or a cubic

packed multilayer structure with about a 1-nm spacing was observed by transmission electron microscopy. In the as-synthesized structures, nanoparticles had a chemically disordered face-centered cubic (fcc) crystal structure and low blocking temperatures (20–30 K) and revealed the superparamagnetic behavior at room temperature, which was due to the low anisotropy of the fcc structure. Annealing at temperatures up to 600°C converted the particles to the high-anisotropy face-centered tetragonal (fct) crystal phase and transformed them into room-temperature nanoscale ferromagnets. The coercivity of these annealed structures depended on the annealing temperature and duration, as well as on the Fe : Pt ratio, and could reach up to 6 kOe. The write/read experiments made on the annealed 120-nm-thick structure of 4-nm Fe$_{48}$Pt$_{52}$ nanoparticles with an in-plane coercive force of 1800 Oe showed that this assembly supported magnetization reversal transitions (bits) at moderate linear densities (up to about 5000 flux changes per mm), which could be read back nondestructively. Higher recording densities are expected for thinner structures (down to a few nanometers). According to the estimations in [5], the nanoparticles in the Fe$_{48}$Pt$_{52}$ sample are characterized by an average anisotropy constant of $5.9 \times 10^7$ erg/cm$^3$.

The authors of the recent work [6] wrote and read bit patterns on arrays of square islands cut with a focused ion beam into granular perpendicular magnetic recording media. Using a static write–read tester, they wrote square-wave bit patterns on arrays of islands with sizes between 60 and 230 nm, matching the recording linear density to the pattern period. These measurements reveal the onset of single-domain behavior for islands smaller than 130 nm, in agreement with magnetic force microscope images.

Our work is focused on the development of a new technology of fabrication and investigation of the properties of metal-containing magnetic nanoparticles less than 10 nm in size and suitable for magnetic and optical recording.

## 2. SAMPLE PREPARATION

### 2.1. Methods for Introducing Nanoparticles into Polymeric Matrices

#### 2.1.1. Thermodestruction of Metal-Containing Compounds

Metallic nanoparticles are introduced into the interstices (voids), which naturally exist in every polymer. These voids arise during the packing of polymer chains, and are located between the crystalline and amorphous parts of micro volumes. We used, as a general route, the thermodestruction of metal-containing compounds (MCC) in polymeric matrices with various sizes of natural interstices. Experiments on kinetics showed that the growth of particles occurs simultaneously in many interstices throughout the polymer. The number and
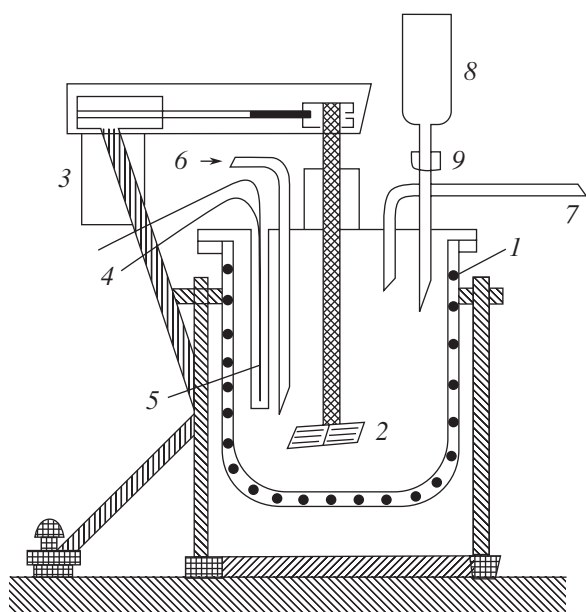
**Fig. 2.1.** Schematic diagram of the high-velocity thermal decomposition apparatus: (*1*) reaction vessel; (*2*) stirrer with electromotor (*3*); (*4*) thermocouple placed in the protective enclosure (*5*); (*6*), (*7*) inlet and outlet tubes for argon, respectively; (*8*) vessel with an MCC solution; and (*9*) dose device.

size of the interstices are specific to each polymeric matrix.

The main method we used to prepare samples containing magnetic nanoparticles in a polymeric matrix was in situ thermodestruction of MCC. Carbonyls, acetates, alkoxides, formates, and some other classes of MCC are applicable. An MCC solution in a volatile solvent is added to a melt of a polymer in mineral oil at the temperature up to 320°C. In the reaction mixture, the chemical reaction of MCC decomposition takes place. At a sufficiently high supersaturation, homogeneous nucleation results in the formation of nanoparticles in polymer interstices. Nucleation is followed by the particle growth, which is restricted by the dimension of polymer interstices. A polymer interstice, in this case, can be regarded as a "nanoreactor" where a nanoparticle forms. In the interstice, the volatile solvent evaporates and metal salt nucleation with one or more solid phases takes place. This is followed at higher temperatures by the decomposition of the metal salts in the particles to form reaction intermediates. As the reaction proceeds, these intermediates diffuse into each other and react to form the nanoparticle with the desired composition.

To obtain the samples by this method, an apparatus for rapid thermal decomposition of MCC was used. The schematic diagram of this setup is shown in Fig. 2.1. During the sample preparation process, an appropriate amount of a polymer was placed in reaction vessel *1* and refined mineral oil was poured into the ves-

sel up to 2/3 of its volume. The vessel can be heated up to 320°C, depending on the type of polymer. The inert gas argon is fed into the reaction vessel until air was completely removed and the entire process is performed in an argon flow. The required temperature is controlled by thermocouple *4*. To provide a better homogeneity of the reaction mixture, electric stirrer *2* was used (with a speed of about 1000 rpm). When the polymer was completely melted in the oil, the solution of the MCC was added through dose device *9* from vessel *8* to the reaction mixture. The reaction mixture was held at a required temperature for about 1 h and cooled to room temperature. In some cases during cooling, the experimental apparatus was placed between the poles of a permanent magnet and the magnetic field strength was changed by adjusting the distance between the magnet poles.

The resulting material was washed with an organic solvent (benzene, hexane) for 12 h at 50°C in order to remove remnant oil and then dried. The resulting dark friable powder was used in further investigations. The metal component content of the samples was determined by the MCC concentration (relative to the polymeric matrix) in the reaction mixture and also was monitored by elemental analysis of the samples.

High-pressure polyethylene (PE), syndiotactic and isotactic polypropylene (PP), and polyamide (PAMD) were used as the polymeric matrix in our investigation. In PE and PP, macromolecules are bonded together by van der Waals forces. However, PP is characterized by a more rigid crystal structure with a lower amorphous phase content. In contrast to PE and PP, PAMD macromolecules are linked by rigid chemical bonds. PAMD is denser and harder than PP and PE, with amorphous regions being almost entirely absent. The melting points of PAMD, PE, and PP are at about 270, 105, and 160°C, respectively.

For some compositions, pellets (plates) about 3 cm in diameter and about 1 mm in thickness were formed. To do this, a powder was put into the appropriate form and pressed under 100 atm at about 150°C.

### 2.1.2. Electrosparking of Metals and Alloys in Styrene

Electrosparking dispersion of alloys of a necessary composition in a monomer results in the formation of corresponding nanoparticles, each of which is covered by a thin film of a polymer. This method has been episodically used to prepare samples containing nanoparticles of complex composition. For example, to prepare samples with NdFeB nanoparticles, we used the electrosparking apparatus schematically shown in Fig. 2.2. The apparatus consists of direct current power source *4*, loading resistor R, capacitor C, thin electrode *2* and massive electrode *1* made of the NdFeB permanent magnet. Both electrodes are immersed in styrene. The nanoparticles are formed as a result of electric erosion in the course of spark discharge between the electrodes

in a dielectric medium (monomeric styrene). Immediately after a particle is formed, a shell of styrene atoms covers its surface and prevents its agglomeration with other particles. Thus, electrosparking results in a fluid with dispersed nanoparticles. Styrene evaporation leads to the formation of a black powder containing about 90 wt % of NdFeB particles.

### 2.2. Preparation of Nanoparticles with Necessary Composition

#### 2.2.1. Homometallic Nanoparticles

To obtain iron nanoparticles in a polymeric matrix, thermodestruction of $Fe(CO)_5$ was used. Thermodestruction (at 240°C for PE and PP and at 320°C for PAMD) involves the following reactions:

$$Fe(CO)_5 \longrightarrow Fe + 5CO \text{ (the main reaction)},$$

$$Fe(CO)_5 \longrightarrow Fe_2O_3 + CO + C,$$

$$Fe(CO)_5 \longrightarrow FeO + CO + C,$$

$$Fe(CO)_5 \longrightarrow FeC + CO + CO_2.$$

In some cases, Fe-containing samples with the PE matrix were prepared by thermodestruction of iron formate $Fe(HCOO)_3$ at 230°C:

$$Fe(HCOO)_3 \longrightarrow Fe + H_2O + CO_2 + CO.$$
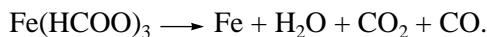
Nickel nanoparticles were formed in the PE matrix upon the thermodestruction of nickel acetate at 240°C:

$$Ni(CH_3COO)_2 \longrightarrow Ni + CO_2 + C_2H_6.$$
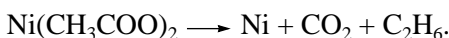
To prepare cobalt nanoparticles in the PE matrix, the thermodestruction of cobalt formate at 300 and 240°C was used:

$$Co(HCOO)_2 \longrightarrow Co + H_2O + CO_2 + CO.$$
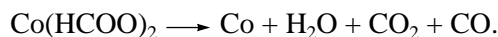
To prepare samples containing various oxide nanoparticles in the PE matrix the following reactions were carried out:
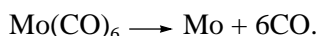(a) for $Fe_2O_3$ nanoparticles (thermodestruction of iron acetate at 240°C),

$$Fe(CH_3COO)_3 \longrightarrow Fe_2O_3 + CO + CO_2 + H_2O;$$

(b) for CoO nanoparticles (thermodestruction of cobalt acetate at 260°C),

$$Co(CH_3COO)_2 \longrightarrow CoO + CO_2 + H_2O + CO.$$

Samples containing 5 wt % Mo were obtained by the thermodestruction of molybdenum carbonyl $Mo(CO)_6$ at 240°C:

$$Mo(CO)_6 \longrightarrow Mo + 6CO.$$

To prepare molybdenum oxide $MoO_3$ in the PE matrix, we used $(NH_4)_2MoO_4$.

The same results were obtained for the other homometallic samples under consideration. It was shown that the particles have a complex composition in the whole range of concentrations (0.5–40 wt % of a metal) and the active interaction of metallic nanoparticles and
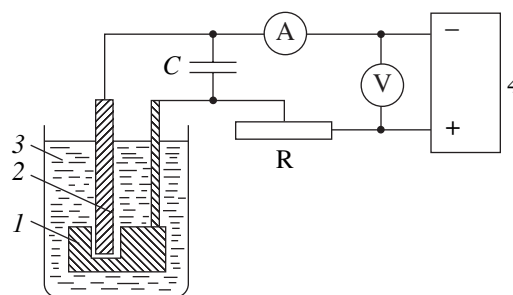


**Fig. 2.2.** Schematic diagram of the electrosparking apparatus.

the polymeric matrix was observed. We noted significant differences in the properties of cluster materials based on the same polymeric matrix but containing various concentrations of the metallic component. All particles contain a metal, metal carbide, and metal oxide. For example, in the case of iron-containing polymers, the major phases in nanoparticles are iron oxide (if a polymer contains less than 30 wt % Fe) and iron carbide (30–40 wt % Fe).

Our preparation method makes it possible to vary the size of nanoparticles from 2 to 6 nm and the interparticle distance from 15 to 9 nm. For high-density storage purposes, the smaller the distance between particles, the better. However, when the particles are closely spaced, dipole–dipole interactions may be significant. In recording media, individual magnetic "bits" should not feel their neighbors or, at least, should be unable to reverse neighbor spins. It is believed that the above values are optimal. In addition, the developed technology gives the possibility for changing the metal concentration in the polymer matrix from 0.1 to 40 wt %, which allows one to considerably vary the interparticle distance. The samples containing the same metal in various matrices were prepared. The metal concentration amounted up to 40 wt %. This made it possible to vary the average distance between the particles in the polymeric matrix and, thus, the number of magnetic particles per unit volume. Many experiments showed that optimum concentration was on the order of 5 wt % of a metal. It was shown that the speed of stirring (in the range of 1000 to 1500 rpm) and the temperature (220–280°C) have no effect on the size of resulting nanoparticles (the difference is no more than 0.5 nm).

#### 2.2.2. Heterometallic Nanoparticles

Bi- and trimetallic nanoparticles and alloys with a more complex composition were obtained either by the decomposition of appropriate heterometallic compounds in a polymer melt or by the introduction of a solution of two (or more) different metal-containing compounds into a polymer melt, the metal ratio being retained in nascent nanoparticles.

Preparation of metal nanoparticles with a complex composition begins with the synthesis of molecular precursors, mixed-metal clusters, which then are decomposed to obtain the required particles. Compounds suitable for these purposes were searched for among compounds with general formula $R_nMM'X_q$, where R is an organic radical; M is Fe, Co, Mn, Cr or other transition metal; M' is Ln, Cu, or Ag; and X is a volatile ligand. The following properties of the compounds were taken into account: (1) stability at room temperature, (2) solubility in appropriate organic solvents, (3) volatility, (4) the nature of thermodestruction products, and (5) availability. In some cases, we developed new preparation routes for the synthesis of mixed-metal clusters, because there are only a few known rational synthesis procedures for preparing compounds with two different metal atoms, and virtually no procedures for tri- or tetrametal clusters. In all, we obtained and characterized more than 60 various heterometallic clusters containing up to four different metal atoms in the cluster core:
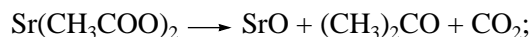
(i) $[F_5MC(CO)_m]$, M = Co, Ni, Pd, Pt, Ru, Mo, Cr, W;

(ii) $[Fe_4MM'C(CO)_m]$, M = Co, Ni, Pd, Pt, Ru, Mo, Cr, W; M' = Co, Ni, Pd, Pt, Ru, Mo, Cr, W;

(iii) $[Fe_3MM'M''C(CO)_m]$, M = Co, Ni, Pd, Pt, Ru, Mo, Cr, W; M' = Co, Ni, Pd, Pt, Ru, Mo, Cr, W; M'' = Co, Ni, Pd, Pt, Ru, Mo, Cr, W.

The clusters were isolated analytically and were spectroscopically pure. The lanthanide clusters $[M(CO)_nL]Ln$ (M = Fe, Co, Mn; Ln = Sm, Yb, Eu) were also isolated and characterized. The Fe–Pt heterometallic clusters were used for preparing Fe–Pt nanoparticles in the PE matrix. The optimum conditions were developed for the decomposition of such compounds in order to introduce heterometallic nanoparticles into a polymeric matrix.

We have devised the method of synthesis of complex nanoparticles upon the simultaneous thermodestruction of two (or more) MCC. In particular, the simultaneous thermodestruction of $Ba(CH_3COO)_2$ (or $Sr(CH_3COO)_2$) and $Fe(CH_3COO)_3$ at 250°C proceeds as follows:

$$Ba(CH_3COO)_2 \longrightarrow BaO + (CH_3)_2CO + CO_2;$$

$$Sr(CH_3COO)_2 \longrightarrow SrO + (CH_3)_2CO + CO_2;$$

$$Fe(CH_3COO)_3 \longrightarrow Fe_2O_3 + CO + CO_2 + H_2O.$$

These reactions were used to obtain $BaFe_2O_4$ and $BaFe_{12}O_{19}$ ferrite nanoparticles by choosing appropriate $Ba(CH_3COO)_2$ and $Fe(CH_3COO)_3$ concentrations in the reaction mixture.

To obtain Fe–Co nanoparticles in the PE matrix, an intermetallic compound was first synthesized by reacting iron pentacarbonyl and $CoCl_2$. Then, it was transformed to a FeCo-containing intermediate with subsequent thermal decomposition at 270–300°C. Another method for the synthesis of Fe–Co nanoparticles was simultaneous thermodestruction of Co and Fe formates $(Co(HCOO)_2$ and $Fe(HCOO)_2)$ at 250°C.

Fe–Sm nanoparticles in the PE matrix were formed by thermal decomposition of $[FeSm(CO)_n]_x$ cluster at 270°C:

$$[FeSm(CO)_n] \longrightarrow Fe + Sm + CO.$$
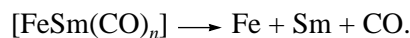
The cluster was synthesized from Fe pentacarbonyl and metallic Sm. Fe–Sm nanoparticles were also obtained by the simultaneous thermodestruction of Fe and Sm formates at 250°C. The composition of the resulting nanoparticles corresponded to the stoichiometric ratio of the components in the initial solution.

Fe–Pt nanoparticles in the PE matrix were synthesized by the reaction of iron pentacarbonyl $Fe(CO)_5$ and $H_2PtCl_6$ at 240°C. The developed methods allow one to fabricate the nanoparticles with a complex composition and the desired ratio of components.

### 2.3. Matrices for the Stabilization of Nanoparticles and Production of the Materials

As is well known, a lot of metallic magnetic nanoparticles are thermodynamically unstable. For their stabilization, we used the following polymers: polyethylene (PE), polypropylene (PP), polytetrafluoroethylene (PTFE), polyamide, polyarylate, polycarbonate, polystyrene, polyethers, poly(phenylene oxide), and siloxane. These polymers have a relatively high thermal and oxidative stability, unique rheological properties, and high dielectric strength. It is also important that these types of polymers are relatively chemically inert. The state-of-the-art level of polymer technology is sufficiently high, therefore, practically, organic polymer matrices are much more preferable from the standpoint of the tasks faced by materials science.

The above-mentioned matrices are typical semicrystalline polymers, with the degree of crystallinity usually lying in the range between 60 and 80%. The crystal part of the polymer structure consists of plates 10–20 μm in size and about 10 nm in thickness. Both the crystal and, particularly, the amorphous parts of polymers contain a significant number of interstices.

Different polymer matrices were used to vary the mean particle size, the width of the particle size distribution, the thickness of the polymer layer on the particle surface, and the extent of the interaction between matrix and nanoparticle. It was shown that the role of the polymeric matrix does not reduce only to the role of the environment for nanoparticles; rather, the surface atoms of nanoparticles efficiently interact with the environmental polymer. To reduce the influence of the matrix on the nanoparticles, the most chemically inert carbon-chain polymers (polyethylene of various degrees of crystallinity, polypropylene of various degrees of stereoregularity, polystyrene) were used for the preparation of the samples. It was shown that sam-
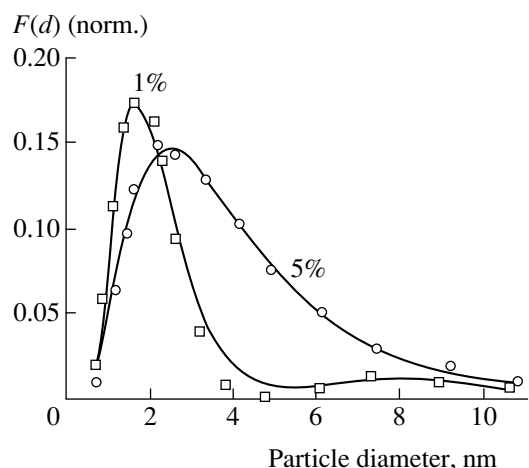
**Fig. 3.1.** Diameter distribution $F(d)$ of nanoparticles in the samples containing 1 wt % and 5 wt % Fe in the PE matrix. The solid line represents the lognormal size distribution function. For the sample with 1 wt % Fe, $F(d) = A_1/(2\pi\sigma_1^2)^{1/2} \times \exp(-\ln^2(d/d_{m1})/2\sigma_1^2) + A_2/(2\pi\sigma_2^2)^{1/2} \times \exp(-\ln^2(d/d_{m2})/2\sigma_2^2)$; $d_{m1} = 2.0 \pm 0.04$ nm; $\sigma_1 = 0.17 \pm 0.01$; $d_{m2} = 8.2 \pm 1.2$ nm; and $\sigma_2 = 0.08 \pm 0.07$. For the sample with 5 wt % Fe, $F(d) = A/(2\pi\sigma^2)^{1/2}\exp(-\ln^2(d/d_m)/2\sigma^2)$; $d_m = 3.57 \pm 0.04$ nm; and $\sigma_1 = 0.171 \pm 0.007$.

ples with a polyethylene matrix satisfied the basic requirements for the recording media best of all.

## 3. X-RAY AND TRANSMISSION ELECTRON MICROSCOPY STUDIES

For the samples' characterization we used small-angle X-ray scattering (SAXS), X-ray RED, EXAFS, and X-ray emission spectroscopy. The X-ray diffraction studies showed that all samples were X-ray amor-
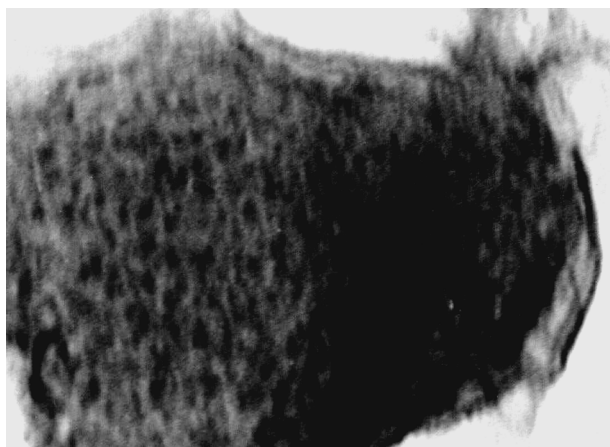
phous. This means that the size of the nanoparticles is less than 10 nm.

SAXS studies showed that magnetic nanoparticles were randomly dispersed in the polymer matrix with lognormal size distribution. Both the two-maximum (bimodal) and one-maximum size distributions were observed. Figure 3.1 shows these two types of distributions for the samples with 1 wt % and 5 wt % Fe in the PE matrix. For the sample containing 1 wt % Fe in the PE matrix, the bimodal lognormal distribution had maxima at a particle diameter of 2.0 nm (±0.04 nm) (the major portion of particles from the total quantity) and 8.2 nm (±1.2 nm). For the 5 wt % Fe sample, the size distribution has one maximum at a particle diameter of 3.57 nm. In any case, the particle diameter did not exceed 10 nm.

The X-ray data concerning particle sizes were confirmed by transmission electron microscopy (TEM). TEM studies were performed using a JEM-100 B-1 electron microscope working at 100 kV. The powder of the sample containing 5 wt % Fe in the PE matrix was dispersed ultrasonically in water. Then, the suspension was placed on a carbon grid and dried. The resulting ultrafine polymeric powder was used to make TEM micrographs (Fig. 3.2). The material was shown to contain nanometer-sized particles with a total absence of a crystal structure. The particles were morphologically mostly nonspherical (ellipsoidal), and their sizes fell within the range from 1.8 to 6.7 nm. The obtained experimental data was fitted by a lognormal distribution function, which gave the average particle diameter (major axis of the ellipse) of 3.6 nm (Fig. 3.3).

The bonding of metal atoms with surrounding atoms and the density of unpaired $3d$ electrons localized on the metal atoms were studied by X-ray emission spectroscopy, which is useful in solving some structural problems and provides information on the atomic orbital of the nearest neighboring atoms or the molecular orbital of the matrix pseudoligand. The phase anal-
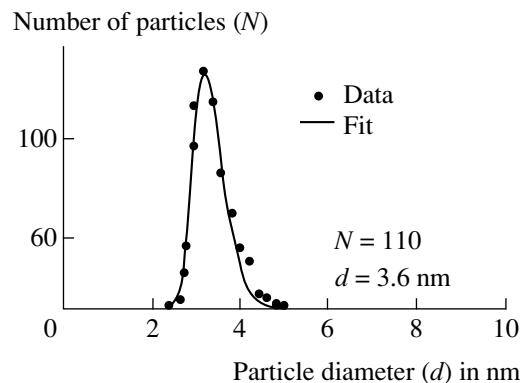


**Fig. 3.2.** TEM micrograph of the sample containing 5 wt % Fe in the PE matrix (1 cm = 10 nm).



**Fig. 3.3.** Lognormal distribution function fit to the experimental particle diameter histogram obtained from TEM data for the sample containing 5 wt % Fe in the PE matrix.

ysis of the samples was carried out by two methods. One of them is the construction of radial electron-density distribution functions obtained from the curve of the X-ray scattering (X-ray RED) intensity, and the second is EXAFS spectroscopy. The advantage of the latter method consists of its selectivity, which allows one to obtain the atomic radial distribution curve for a local arrangement of a given chemical element in the sample. Both methods give interatomic distances (*r*) and coordination numbers (*Z*). X-ray emission spectra showed that the major part of Fe nanoparticle (about 70%) consisted of $\gamma$-Fe$_2$O$_3$ and also pointed to the presence of the bonds between iron atoms at the nanoparticle surface and the surrounding matrix (Fe–O–CH$_2$, FeOH–CH$_2$OH, etc.). These data allow one to conclude that nanoparticles are fixed in the matrix and cannot rotate in an external magnetic field.

Preliminary studies of samples with various polymeric matrices showed that the phase state of the nano-sized metal particles is strongly determined by the matrix, the types of bonds of the particles with the matrix, and the presence (or absence) of active functional groups. In particular, X-ray diffraction patterns (Cu$K_\alpha$ radiation, $2\theta$ range from $0°$ to $35°$) were measured for the samples with 1, 2, 3, 4, 5, 10, and 20 wt % Fe in paraffin, a simple oligomeric matrix.

According to the data obtained, an increase in the iron concentration leads to a decrease in the intensity of the reflections from paraffin. This indicates an essential structural change in the paraffin matrix itself. All the reflections at angles up to $15°$ are shifted toward smaller scattering angles. This is connected with the increase in the interplanar spacings and the increase in the sizes of the crystallites in paraffin. The latter is possible only because of the bonding of the molecules of paraffin into more complicated structures due to the interaction with nanoparticles. Increasing the Fe concentration in paraffin also results in the appearance of two new reflections, one of which is related to $\alpha$-Fe and another, to Fe$_2$O$_3$.

The X-ray diffraction patterns of the samples containing Fe nanoparticles in the PE matrix (with concentrations from 3 to 30 wt % Fe) in most cases have no additional maxima that can be related to nanoparticles. This points to an irregular, probably amorphous, structure of nanoparticles. However, in some cases, especially after heat treatment, new reflections appeared, which can be related to Fe oxides and carbides.

On the basis of diffraction data, the size distribution of Fe nanoparticles in paraffin matrix was obtained. Three samples were studied: 10 wt % Fe obtained by prolonged cooling (sample 1), 10 wt % Fe obtained by quick cooling (quenching) (sample 2), and 20 wt % Fe obtained by quenching (sample 3). The distribution had a lognormal character and a wide maximum at a particle diameter of about 2.8 nm for sample 1, a narrower maximum at ~2.4 nm for sample 2, and a small wide maximum at ~9 nm for sample 3.

The obtained data revealed general lognormal nanoparticle size distribution for Fe-containing samples with different polymeric matrices. With the increasing Fe concentration in the sample, the particle diameter increased. For samples containing 1 wt % Fe, the diameter of a particle was about 2 nm, and for the samples with higher Fe concentrations, it reached about 4 nm.

## 4. THERMAL STABILITY AND MECHANICAL PROPERTIES OF THE SAMPLES

The stability of the mechanical properties of the investigated materials upon temperature changes is of crucial importance because of their possible use in applications where hazardous thermal conditions exist.

Herein, we studied thermally induced mechanical stresses in rectangular polyethylene plates (with dimensions $1.0 \times 2.0 \times 10.0$ mm) when the sample was thermally cycled at a rate of 1 K/min between 100 and $-70°$C. As a typical system, the sample with 5 wt % Fe in the PE matrix was chosen, but samples with 10 and 15 wt % Fe were also studied.

For the stress measurements, we used the method based on the experimental technique of L.M. Vinogradova *et al.* [7]. The polymer glass transition temperature $T_g$ was determined using a standard thermal analyzer at a heating rate of 10 K/min.

The experimental measurements showed that the $T_g$ value of the sample containing 5 wt % Fe was $30°$C higher than that of pure polyethylene. This fact can be explained by the increase in the effective molecular weight of PE, which is caused by the increase in the degree of cross-linking in the polymeric matrix due to interactions with the nanoparticles. A further increase in the Fe concentration results in a decrease in $T_g$, which is usual for composite materials.

When a rectangular test sample is heated (or cooled), its surface bends from the initial horizontal position. Figure 4.1 shows the temperature dependence of such a bending in the sample with 5 wt % Fe measured on cooling from 100 to $-70°$C, exposure for 20 minutes at this temperature, and subsequent heating back to $100°$C. Analogous measurements were made for the samples containing 10 and 15 wt % Fe. After the temperature cycle was completed, the surface of the sample returned to its original position. Our experimental findings show that the mechanical properties of the studied polyethylene samples containing Fe nanoparticles should be stable in the temperature range from $-40$ to $+50°$C, which is usual for most electronic and information storage system applications.

Our investigations show that implantation of metallic nanoparticles into polymeric matrices, especially in the concentration range of about 5 wt %, also results in a small but quite real increase in their resistance to destruction by heat. For example, the initial temperature of polyethylene heat destruction rises to $80°$C after

the implantation of metallic nanoparticles. This is enough for most practical tasks so that it is not necessary to use special thermostable polymers as a matrix for nanoparticles.

The processing of the polymeric materials to obtain desired forms and articles is very important from the technological standpoint. Typical polymer processing procedures are drawing, bending, rolling, upsetting, stamping, coining, hydroforming, molding, and ram or hydrostatic extrusion. Most of these methods can be used for the fabrication of articles of various designs from powders containing metallic nanoparticles in the polymeric matrix. In this connection, it is important to compare the extrusion behavior of these powders to that of the initial polymers.

The extrusion experiments were made with the help of the ram extrusion method, in which the pressure was applied directly to the semicrystalline billet using a piston. The temperature of extrusion and the load of the ram were 190°C and 2.16 kg, respectively. The melt flow index (MFI) was used as a measure of the extrusion properties (extrusion velocity) of samples. Table 4.1 shows the results obtained for the samples containing 5 and 20 wt % Fe in the matrix of high-pressure polyethylene (which was used in our investigation) together with the MFI values for pure high-pressure (HPPE) and low-pressure polyethylene (LPPE). As one can see from the table, the introduction of the metal into the matrix has a strong effect on the extrusion behavior. The difference in extrusion velocity decreases with increasing the metal content, which points to the increase in the rigidity of polymeric materials after the introduction of metallic nanoparticles.

## 5. MÖSSBAUER INVESTIGATIONS

Mössbauer spectra were recorded at room temperature on an MS1101E constant-acceleration spectrometer (Institute of Radium Studies, Mir Regional Center of Science and Technology). $\gamma$-radiation sources were $^{57}Co$ in chromium metal matrices with activities up to 10 mCi (Cyclotron Co., Ltd., Obninsk, Russia) were used. Isomer shifts were referenced to $\alpha$-Fe.

Mössbauer spectroscopy makes it possible to determine the phase composition of the samples and to estimate the particle sizes. Mössbauer studies of those samples containing Fe nanoparticles in polyethylene and polypropylene (syndiotactic and isotactic) matrices.

Iron nanoparticles were found to contain at least three different phases: pure iron, iron(III) oxide ($Fe_2O_3$), and various iron carbides. The pure iron con-
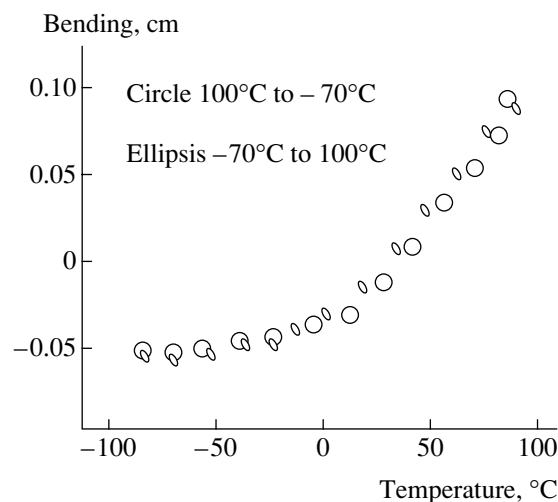


**Fig. 4.1.** Temperature dependence of the sample surface bending for the sample containing 5 wt % Fe in the PE matrix.

tent of the samples with 0.20, 4.54, 7.92 wt % Fe in the PE matrix was in the range from 5 to 25% depending on the iron content and decreased while the overall iron content increased. The relative quantity of iron oxide $Fe_2O_3$ was about 60% in all three samples and practically did not change with the Fe content. The remaining part of Fe nanoparticles was iron carbides. A representative Mössbauer spectrum of Fe-containing samples is shown in Fig. 5.1. It can be satisfactorily described as a superposition of four sextets corresponding to $\alpha$-Fe and two doublets corresponding to $\gamma$-$Fe_2O_3$ (the absence of hyperfine interaction indicates that the particles should not exceed 60 Å in size). The relative area of spectrum corresponding to the sextets increased on cooling the samples to 78 K.

To clarify the mechanisms of the formation of iron oxide and other compounds inside a nanoparticle and the interaction of nanoparticles with outside media, we studied the Mössbauer spectra of groups of samples with 5 wt % Fe in the PE matrix obtained and processed under different conditions: the powder synthesized and packed in a hermetic shell in an argon atmosphere (group 1), the powder synthesized in the same way and then exposed to air for different periods of time (group 2), and the pellets (20 mm in diameter and 1 mm thick) pressed from the same powder in an argon atmosphere and then exposed to air (group 3). It was found that the Mössbauer spectra of the group 1 samples did not change with time. The Mössbauer spectra of all samples pointed to the presence of $\alpha$-Fe, iron(III)

**Table 4.1.** Extrusion properties of pristine PE matrices (high-pressure (HPPE) and low-pressure (LPPE) polyethylene) and of the samples containing 5 and 20 wt % Fe

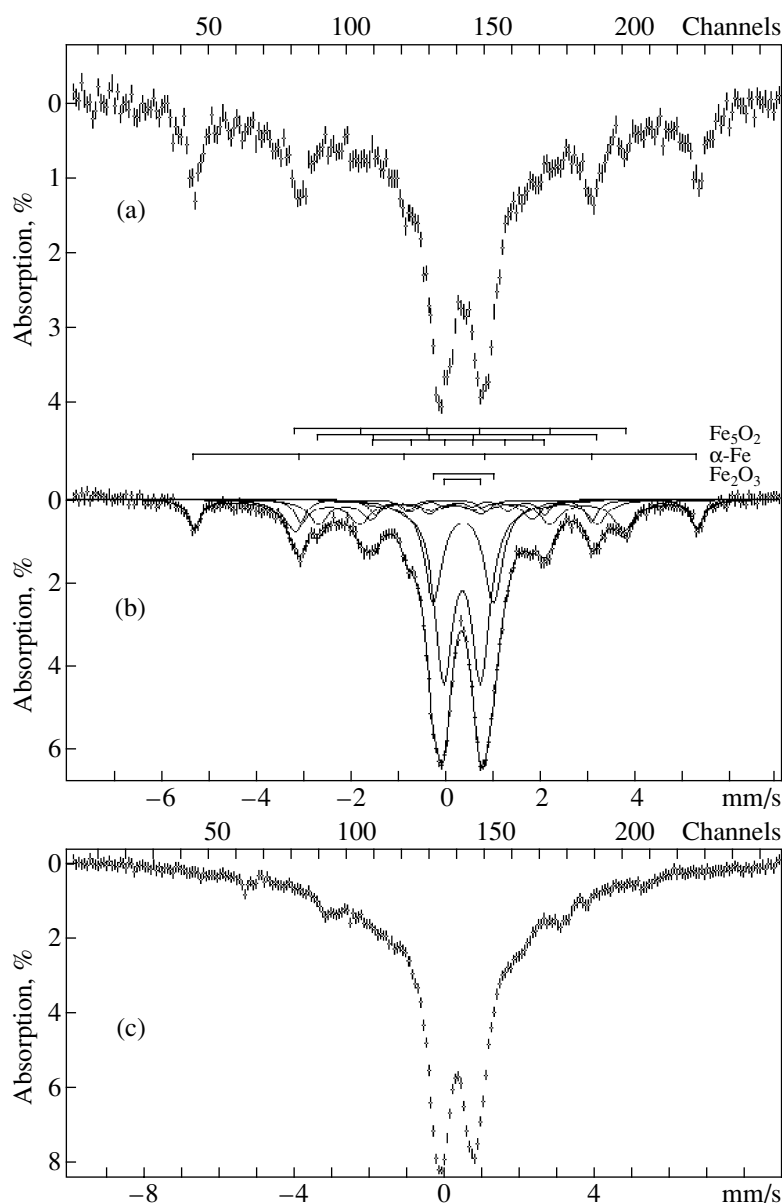| Sample | LPPE | HPPE | HPPE + 20 wt % Fe | HPPE + 5 wt % Fe |
|---|---|---|---|---|
| MFI (g) | 9.6 | 6.49 | 0.049 | 0.51 |

**Fig. 5.1.** Mössbauer spectra of the sample containing (a) 0.20, (b) 4.54, and (c) 7.92 wt % Fe in the PE matrix.

oxide, and some amounts of iron(II) oxide (FeO). During exposure to air, the content of iron(II) oxide decreased and that of iron(III) oxide increased (Fig. 5.2). On the basis of obtained Mössbauer data, it was concluded that the formation of iron(III) oxide took place at the stage of the synthesis of the samples (the source of oxygen was probably carbon(II) oxide) and also upon the interaction of the nanoparticles with air oxygen penetrating into the samples through the matrix. The results obtained for the pressed pellets did not differ from the data for the powder samples.

The Mössbauer spectra of the samples containing Fe nanoparticles in the polypropylene (PP) matrix were also measured. PP is more rigid than PE, with a lower content of the amorphous part. In PP, the interstices in which nanoparticles are formed are less scattered in size. A higher rigidity of PP and a smaller difference in interstice sizes in it manifest themselves in well-defined narrower spectra. The samples with 5.41, 5.8, 9.7, 11.8, 28.4, 33.7 wt % Fe in syndiotactic and isotactic PP were studied. The composition of the nanoparticles was found to be the same as in the case of the PE matrix reported above: $\alpha$-Fe, $Fe_2O_3$, and carbides (such as $Fe_3C$ and $Fe_5C_2$) (Fig. 5.3). The content of pure iron decreased and the content of carbides increased with the increase of the total iron content (the sample with 11.8 wt % Fe contained about 20% of carbides; and the sample with 33.7 wt % Fe, about 72%). The content of $Fe_2O_3$ changed from ~77% in the sample with 11.8 wt % Fe, to ~25.4% in the sample with 33.7 wt % Fe.
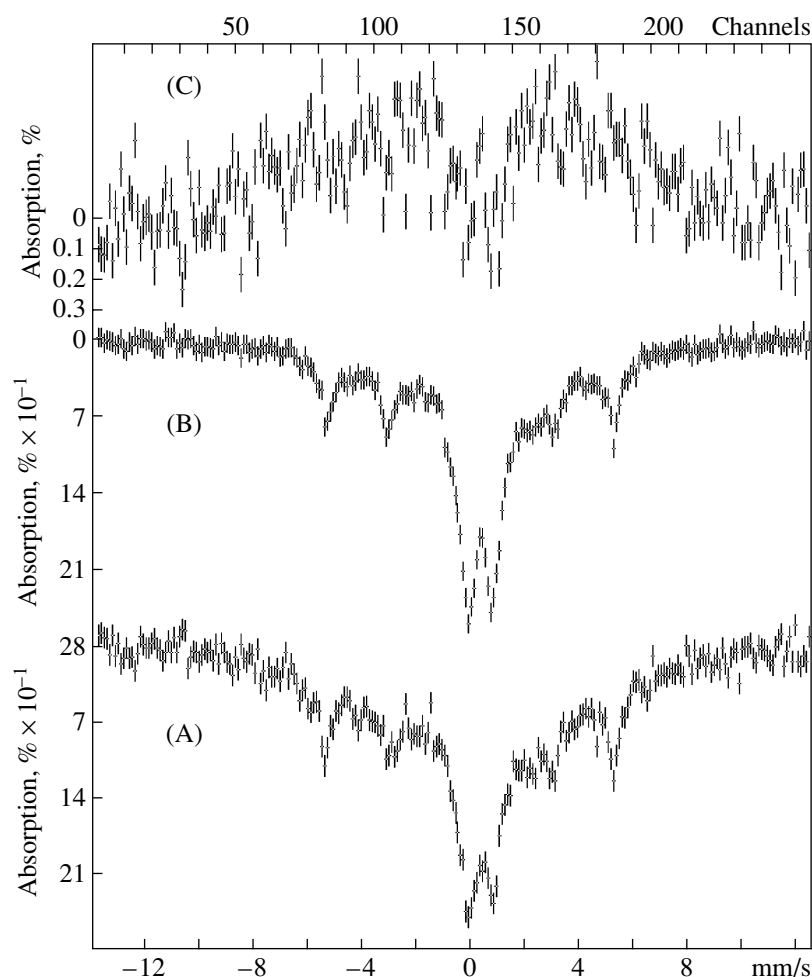
**Fig. 5.2.** (A) Mössbauer spectrum of the powder sample with 5 wt % Fe in the PE matrix prepared and packed in a hermetic shell in an argon atmosphere, (B) the spectrum of the sample exposed to air, and (C) the spectrum obtained by subtraction of the first spectrum from the second.

So, one can conclude that the main features of the composition of nanoparticles in the PP matrix are almost the same as in the PE one.

Mössbauer spectra were also measured for a series of samples containing 5 wt % Fe in the PE matrix subjected to heat treatment in air at temperatures up to 280°C for up to 6 h. According to the Mössbauer spectra, the original sample contained about 24% $\alpha$-Fe and significant amounts of iron(III) oxide displayed as a central doublet. Visible changes were not observed in the spectra up to 100°C. Heating the material at 200°C for 1 h resulted in the oxidation of the major portion of metallic iron. As a result of this process, the noticeable central doublet of iron(III) oxide was observed in the Mössbauer spectrum. Heat treatment at higher temperatures led to the appearance of a new sextet with the following parameters: $\delta = 0.60 + 0.04$ mm/s, $\Delta = 0.00 + 0.08$ mm/s, and $H = 429 \pm 3$ kOe. These parameters are unusual for the oxygen-containing systems of iron. Indeed, the chemical shift value corresponds to a fractional oxidation number of iron (+2.5). An analogous situation was observed, for example, for the well-documented $Fe_3O_4$; however, this oxide gives rise to two sextets with $\delta = 0.26$ and $\delta = 0.66$ mm/s, corresponding to the ions of iron(III) and iron(II) in tetra- and octahedral surroundings, respectively. In our case, only one set of lines was observed and the value of the magnetic field at iron nuclei was significantly lower than that for the $Fe_3O_4$ (493 and 460 kOe, respectively). Based on the experimental results we can speak about the partial reduction of iron(III) oxide on heating to 280°C. So, our findings allow us to conclude that heating the Fe-containing material in air first leads to the oxidation of the metal to iron(III) oxide and further heating results in its reduction to the oxide containing $Fe^{+2.5}$.

Figure 5.4 shows the Mössbauer spectrum of the sample containing 5 wt % Fe in the PE matrix characterized by a high coercive force (about 950 Oe). The Mössbauer spectrum of the sample is satisfactorily described by four subspectra consisting of two magnetic sextets and two doublets corresponding to metal iron and iron oxides (Table 5.1). The parameters of sex-
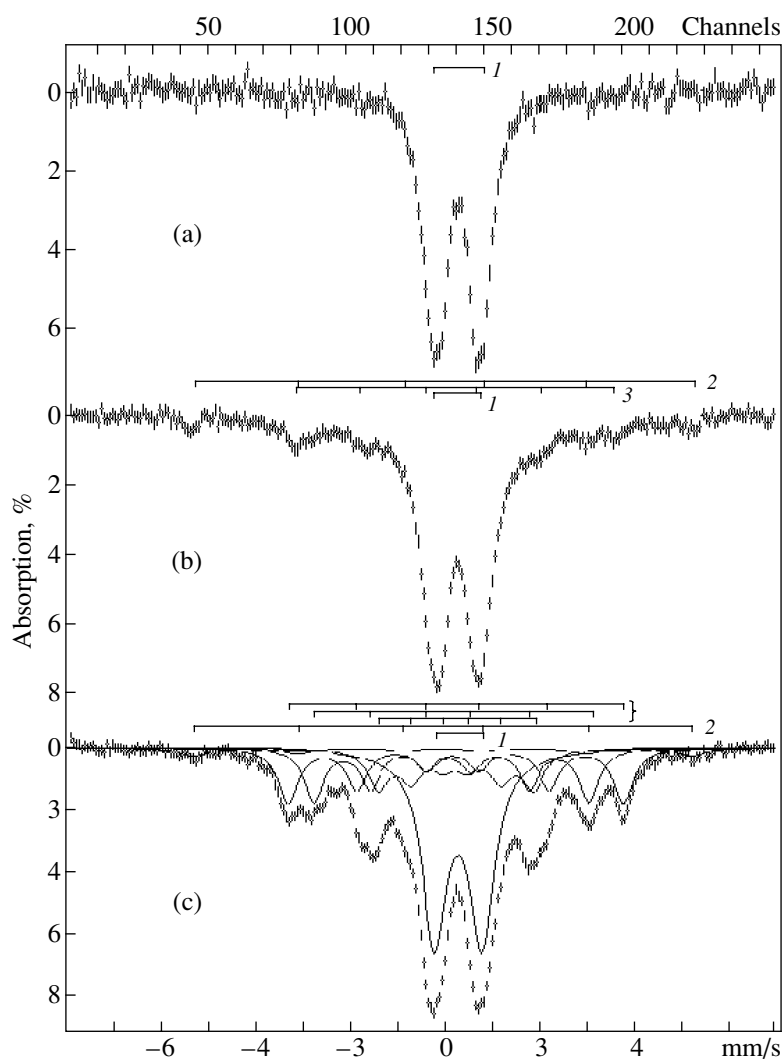
GUBIN *et al.*



**Fig. 5.3.** Mössbauer spectra of the samples containing (a) 5.8, (b) 11.8, and (c) 28.4 wt % Fe in the PP matrix: (*1*) $\alpha$-Fe$_2$O$_3$, (*2*) $\alpha$-Fe, (*3*) Fe$_3$C, and (*4*) Fe$_5$C$_2$.
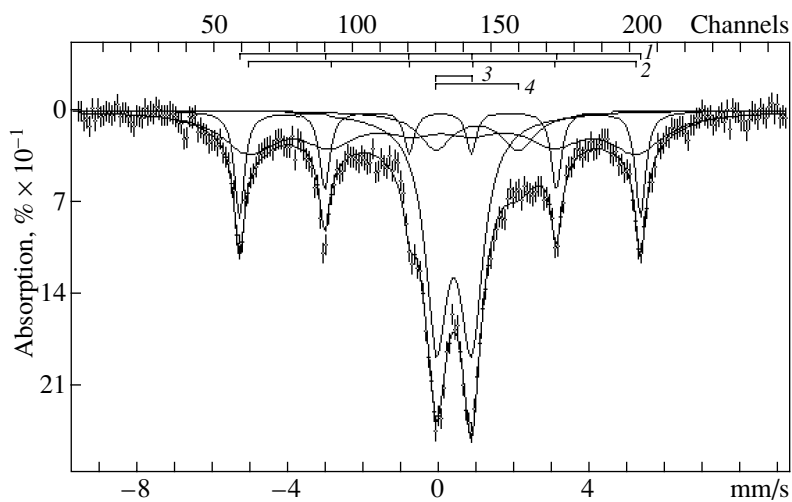


**Fig. 5.4.** Mössbauer spectrum of the sample containing 5 wt % Fe in the PE matrix with a high value of the coercive force (*1*, *2*) Fe; (*3*) Fe$_2$O$_3$; (*4*) FeO.

tet line *1* are similar to the corresponding parameters for α-Fe. The nanoparticles can be considered to consist of a core with a structure typical of bulk iron. Sextet line *2* has a smaller value of the hyperfine field and a greater width. It corresponds to the metal iron with a lower degree of long-range order (more amorphous). The amount of this iron in the nanoparticles is less than that of α-Fe. The central resolved quadrupole splitting line *3* with the maximal relative area most likely belongs to γ-Fe$_2$O$_3$. Iron(III) oxide can form a shell on the particle surface. The second doublet (line *4*), by its parameters, can be assigned to iron(II) oxide contained in the intermediate layer between the metal core of a particle and its shell formed by iron(III) oxide.

## 6. ELECTRON PARAMAGNETIC RESONANCE (EPR) STUDIES

EPR spectra were recorded on a Varian E-109 spectrometer operating at a frequency of ~9.2 GHz (X-band). A magnetic field up to 5 kOe was created by a Varian Associates 12 in. electromagnet. A standard field modulation (100 kHz) and phase-sensitive detector techniques were used to detect the output signal corresponded to the field derivative of the absorbed power ($P' = dP/dH$). The temperature was controlled by a flow helium cryostat system (Oxford Instruments, USA) from 4.2 to about 300 K and by a nitrogen variable temperature system E-257 (Varian) from 120 to about 500 K. Three principal characteristics of EPR spectra were determined: the resonance field $H_r$, the peak-to-peak line width of the resonance $\Delta H$, and the signal amplitude. The resonance field was defined as the field at the midpoint between the maximum and minimum in the plot of the output signal versus the external magnetic field. The signal amplitude was measured as the difference between the maximum and minimum in the spectrum. The effective value of *g*-factor was determined by the relation $g = 2H_e/H_r$, where $H_e$ is the resonance field corresponding to a free-spin marker like diphenylpicrylhydrazyl.

Samples containing Fe$_2$O$_3$ in a wide range of concentrations (from 1 to 30 wt %) in the PE matrix, Fe in the PE and polyamide (PAMD) matrices, Ni in the PE matrix, and BaFe$_2$O$_4$ and BaFe$_{12}$O$_{19}$ in the PE matrix were studied by EPR. The basic results of the investigations have been reported in [8–10].
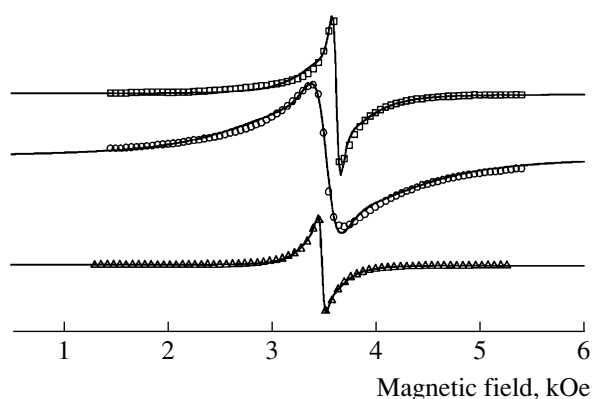


**Fig. 6.1.** EPR spectra of the samples containing 1.4 and 7.1 wt % Fe$_2$O$_3$ in the PE matrix. Experimental data are presented by squares for 1.4 wt % Fe$_2$O$_3$ sample at 300 K; circles ($T = 300$ K) and triangles ($T = 500$ K) for 7.1 wt % Fe$_2$O$_3$ sample. Solid lines are the results of numerical fitting to Lorentzian line shape.

The EPR spectra of all studied samples have general features. At room temperatures, they show a "two-line pattern" typical of a superparamagnetic resonance spectrum [11]. This spectrum can be represented by a broad line superimposed on a narrow line. The relative intensity of these lines depends on the particle size and shape distributions and on the magnetic anisotropy magnitude and can change with temperature [11, 12]. According to the literature data [13], narrow and broad EPR signals in nanoparticle systems are attributed to superparamagnetic and ferromagnetic resonance, respectively.

### 6.1. Iron Oxide and Iron-Based Samples

Figures 6.1–6.3 present characteristic results obtained for the samples containing 1.4 wt % Fe$_2$O$_3$ in the PE matrix. Figures 6.1 and 6.2 show the EPR spectra of these samples and Fig. 6.3 shows the plots of the EPR linewidth and signal amplitude versus temperature. As one can see from Figs. 6.1 and 6.2, a narrow EPR line at $g \approx 2.0$ dominates the spectrum at high temperatures. On cooling, a broad ($\Delta H > 1$ kOe) line builds up and becomes prevalent below about 20 K. At all studied temperatures, both the narrow and broad lines decrease in amplitude and broaden with the cooling of the sample. An analogous behavior of EPR spectra is

**Table 5.1.** Parameters of the Mössbauer spectrum of the sample containing 5 wt % Fe in the PE matrix characterized by a high coercive force (δ, isomer shift; Δ, quadrupole splitting; $H$, hyperfine field; Γ, line width)

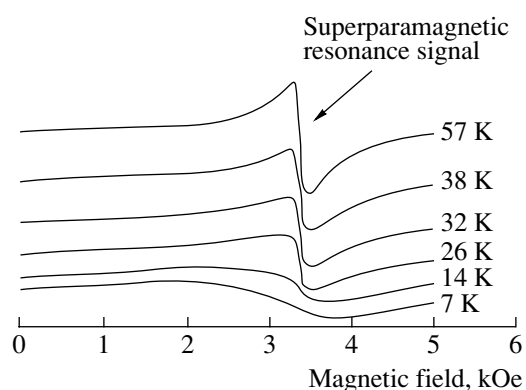| Line number | δ, mm/s | Δ, mm/s | $H$, kOe | Γ, mm/s | Relative area, % |
|:---:|:---:|:---:|:---:|:---:|:---:|
| *1* | $0.05 \pm 0.01$ | $-0.01 \pm 0.01$ | $331 \pm 1$ | $0.32 \pm 0.03$ | 18.59 |
| *2* | $0.10 \pm 0.04$ | $0.02 \pm 0.06$ | $318 \pm 4$ | $1.45 \pm 0.14$ | 29.41 |
| *3* | $0.43 \pm 0.01$ | $0.95 \pm 0.02$ | | $0.74 \pm 0.02$ | 40.96 |
| *4* | $1.02 \pm 0.07$ | $2.18 \pm 0.13$ | | $1.12 \pm 0.12$ | 11.04 |

**Fig. 6.2.** EPR spectra of the sample containing 1.4 wt % $Fe_2O_3$ in the PE matrix at different temperatures.
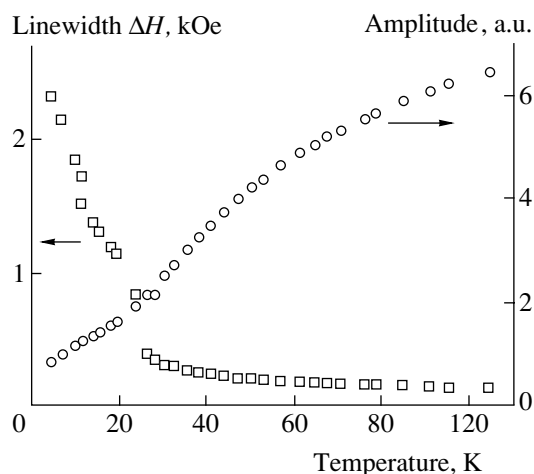


**Fig. 6.3.** Temperature dependence of the EPR linewidth and signal amplitude for the sample containing 1.4 wt % $Fe_2O_3$ in the PE matrix.

observed for the sample containing 7.1 wt % $Fe_2O_3$ in the PE matrix, although the broad EPR line becomes dominant at higher temperatures (at about 70 K).

In the well-developed model of EPR in bulk materials [14, 15], the resonance field $H_r$ of a sample magnetized to saturation by a strong external field is a function of the $g$-factor, the magnetocrystalline anisotropy field, and the demagnetization field and can be presented as

$$H_r = h\nu/g\mu_B - \alpha H_a + H_s, \qquad (1)$$

$$H_a = \alpha|K|/M, \qquad (1a)$$

$$H_s = -\Delta NM, \qquad (1b)$$

where $H_a$ is the anisotropy field, $H_s$ is the demagnetization field, $K$ is the anisotropy constant, $\alpha$ is a factor depending only on the angles between the applied field and the crystallographic axes, $M$ is the sample magnetization, $\Delta N$ is the anisotropy form factor and is a function of sample dimensions, $h\nu/g\mu_B$ is the resonance

field in the paramagnetic limit, $\mu_B$ is Bohr magneton, and $\nu$ is frequency.

With the application of this "bulk" model to nanoparticle systems, several assumptions are usually made [14, 16, 17]. A nanoparticle system is considered to be a coherent assembly of small noninteracting particles with the same intrinsic magnetization $M_s$, the same volume $V$, and the same anisotropy constant $K$, embedded in a diamagnetic matrix. The applied field is suggested to be much stronger than the anisotropy field, and the particles are suggested to have the shape of an ellipsoid of revolution with the applied field directed along one of the principal axes of the ellipsoid. Under these conditions, in the case of nanoparticles with a uniaxial magnetic anisotropy, the relation for the resonance field can be written as

$$H_r = h\nu/g\mu_B - \alpha(|K|/M)(1 - 2/x) + \Delta NL(x), \qquad (2)$$

where $x = VHM_s/k_BT$, $L(x)$ is the Langevin function and $k_B$ is the Boltzmann constant [14]. At high temperatures ($x \ll 1$), anisotropy and demagnetization fields for nanoparticle systems tend to zero. In this case, the EPR line is observed at $H_r \approx h\nu/g\mu_B$ and is narrowed by rapid superparamagnetic fluctuations. This is so-called superparamagnetic resonance [13]. At low temperatures, $H_a$ and $H_s$ tend to their bulk values and the fluctuations are suppressed and slowed down; therefore, $H_r$ changes from its initial value and a broad signal of the ferromagnetic resonance should be observed.

The model of electron paramagnetic resonance in the nanoparticle systems described above makes it possible to explain the EPR spectra obtained and their temperature dependence. According to the experimental data (see Figs. 6.1–6.3 as an example), the decrease in the intensity of the narrow signal is accompanied by the growth and low-field shift of the broad one. At high temperatures, weakly interacting nanoparticles give rise to the EPR signal, which is narrowed by superparamagnetic fluctuations. On cooling, nanoparticles undergo transition to the stable state (blocking state) and give rise to a rather broad resonance signal of the ferromagnetic type. For the sample containing 1.4 wt % $Fe_2O_3$, the average particle diameter $d_m$ is about 2 nm and the transformation of EPR spectra from "narrow" to "broad" happens below about 25 K (Figs. 6.2, 6.3). For the sample containing 7.1 wt % $Fe_2O_3$ with larger particles ($d_m = 3.6$ nm), this transformation was observed below about 70 K.

The features and temperature behavior described above are common for the samples containing $Fe_2O_3$ nanoparticles in a polymeric matrix studied in this work. For the samples with higher Fe concentrations in the PE matrix (28 and 40 wt % $Fe_2O_3$), the EPR signals are essentially broader than for the above samples with low Fe concentrations. This can be associated with the rather large sizes of nanoparticles in these samples [18]. Estimations made in [13, 19] showed that the average particle diameter should be around 2.6 nm for a line-

width of about 170 Oe. On the other hand, the observed EPR line broadening may by connected with the increase in the temperature corresponding to the transition to the blocking state (blocking temperatures) in the samples with higher magnetic component concentrations.

The Néel theory of superparamagnetic relaxation gives the relation

$$T_b^{\mathrm{EPR}} / T_b^{\mathrm{m}} = \ln(\tau_m/\tau_0)/\ln(\tau_{\mathrm{EPR}}/\tau_0), \tag{3}$$

where $T_b^{\mathrm{m}}$ is the blocking temperature obtained from magnetic measurements, for which the characteristic time of measurement $\tau_m$ is about $10^2$ s; $T_b^{\mathrm{EPR}}$ is the blocking temperature obtained from EPR measurements (at this temperature, relaxation time $\tau$ of a superparamagnetic system is equal to the characteristic time of EPR measurement $\tau_{\mathrm{EPR}} \approx 10^{-10}$ s); and $\tau_0$ is on the order of $10^{-10}$–$10^{-12}$ s [20, 21]. According to Eq. (3), $T_b^{\mathrm{EPR}}$ can be about 6 times larger than $T_b^{\mathrm{m}}$ and the broadening of EPR lines should start at about $2T_b$ [22].

Significant EPR line broadening was observed at low temperatures (below about 25 K) in the samples with 1.4, 7.1, and 40 wt % $Fe_2O_3$ in the PE matrix. This behavior can be related to the emergence of the spin glass (or antiferromagnetic) state in the surface layer of $Fe_2O_3$ in the nanoparticle. According to the literature data, many experiments indicate that $\gamma$-$Fe_2O_3$ nanoparticles have a surface layer, which undergoes a spinglass-like transition near 50 K [23–26]. The existence of the spin glass (or antiferromagnetic) layer on the surface of the ferromagnetic core can lead to the emergence of unidirectional exchange anisotropy [24, 27]. This anisotropy additionally contributes to the anisotropy field $H_a$ and, consequently, has an influence on the EPR spectra. In [24] it was found that the additional exchange anisotropy field starts to increase in a $\gamma$-$Fe_2O_3$ nanoparticle below 25 K. The general character of EPR linewidth temperature dependence observed in our experiments correlates with that of the exchange anisotropy field [24].

The temperature dependence of the EPR spectrum for the sample containing 5 wt % $Fe_2O_3$ in the PE matrix was investigated in detail (Figs. 6.4, 6.5). In the room-temperature spectrum, the broad line characterized by the peak-to-peak line width $\Delta H \approx 850$ Oe and an effective $g$ value of approximately 2.07 predominates. At low temperatures, the EPR spectra of $Fe_2O_3$ changed significantly (Fig. 6.5). On cooling below 100 K down to the lowest reached temperature (about 5.5 K), broad line $S1$ behaves as a typical superparamagnetic resonance line, namely, the linewidth $\Delta H$ monotonically increases while the signal amplitude $A$ decreases. Below about 50 K, new resonances, $S2$ and $S3$, appeared in the spectra of $Fe_2O_3$. These lines became more noticeable under sample cooling. Their
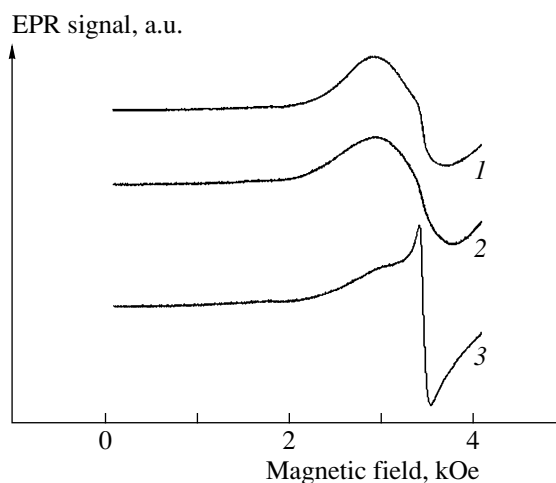


**Fig. 6.4.** Room-temperature EPR spectra for the samples containing 5 wt % $Fe_2O_3$ (curve *1*), $BaFe_2O_4$ (curve *2*), and $BaFe_{12}O_{19}$ (curve *3*) in the PE matrix.
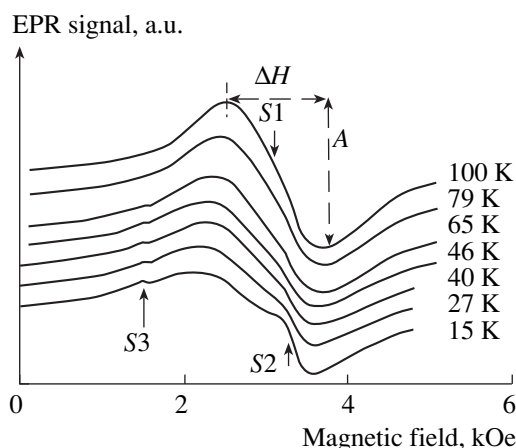


**Fig. 6.5.** EPR spectra of the sample containing 5 wt % $Fe_2O_3$ in the PE matrix. $\Delta H$ and $A$ are the peak-to-peak linewidth and the EPR signal amplitude, correspondingly.

effective $g$ values were temperature independent and were equal to 2.02 and 4.3 for $S2$ and $S3$, respectively. The amplitude of the $S2$ line increased and its linewidth decreased with decreasing temperature. The dependences $\Delta H(T)$ and $A(T)$ of the $S3$ line revealed maxima at about 7.5 and 5.5 K, respectively. The strongest EPR signal $S1$ in the spectrum of the $Fe_2O_3$ sample is very similar to that observed in [28, 29] in chemically prepared $\gamma$-$Fe_2O_3$ nanoparticles of ferrofluids. Since $S1$ has a typical superparamagnetic character, one can presume that this is due to a ferrimagnetic phase like $\gamma$-$Fe_2O_3$. The value $g = 4.3$ for line $S3$ is characteristic of the high-spin state of $Fe^{3+}$ in the rhombic crystal field [30, 31]. A significant deviation from axial symmetry can be realized in rhombohedral $\alpha$-$Fe_2O_3$. The observed maxima in the $\Delta H(T)$ and $A(T)$ curves of the $S3$ line are evidence of an antiferromagnetic transition [32]. This
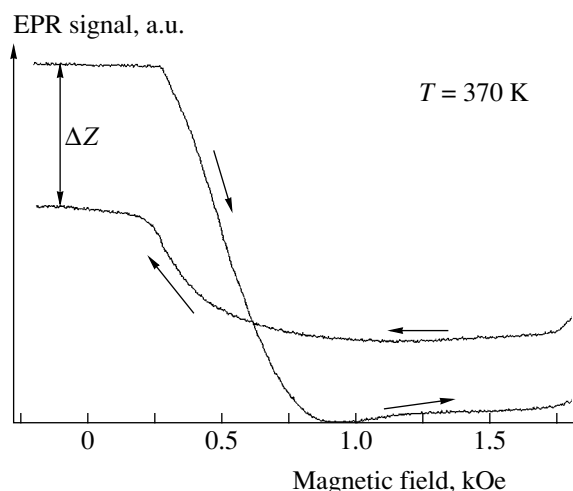
EPR signal, a.u.



**Fig. 6.6.** Hysteresis of the EPR signal at low fields in the plate sample containing 5 wt % Fe in the PE matrix.

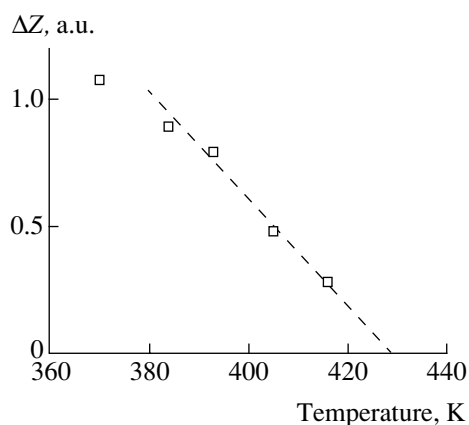$\Delta Z$, a.u.



Temperature, K

**Fig. 6.7.** Temperature dependence of the EPR signal shift in zero field at high temperatures for the plate sample containing 5 wt % Fe in PE matrix.

can be a Morin-type transition shifted to a low-temperature region [33]. Therefore, the S3 signal can be attributed to $\alpha$ phase of $Fe_2O_3$ nanoparticles. On the other hand, the paramagnetic signal S2 ($g = 2.02$) may be due to the octahedral $Fe^{3+}$ sites in a spinel structure of the $\gamma$ phase. The presence of oxygen vacancies near such centers could break the exchange interactions that provide the ferrimagnetic properties of $\gamma$-$Fe_2O_3$.

Remanent magnetization ($M_r$) and its temperature dependence are very important parameters for magnetic recording. To study the temperature behavior of remanent magnetization in the system of nanoparticles in a polymeric matrix, the zero-field shift of EPR signal for the plate sample containing 5 wt % Fe in the PE matrix was measured.

Many materials with ferromagnetic ordering give rise to a characteristic broad line in a low-field region (with $g \approx 8$–10), which is usually attributed to a ferromagnetic resonance (FMR) signal. An analogous FMR

signal was observed in the studied samples containing magnetic nanoparticles in polymeric matrices. The signal has a hysteretic behavior, which is registered during increasing and decreasing the external magnetic field. The measurements were made as follows. A nonmagnetized sample was placed in the cavity of an experimental EPR spectrometer in the external magnetic field $H = 0$. Then, the maximum possible magnetic field was applied and switched off again, which led to sample magnetization. Next, the sample was turned over, so that its magnetization vector became opposite to the direction of the static magnetic field in the spectrometer. Then, the EPR spectrum was recorded while the external magnetic field was changed from zero to 3 kOe and then back to zero. At the end of the measurement, the magnetization of the sample was directed roughly opposite to its initial direction. The difference in the EPR signal value at the beginning and at the end of the measurement when $H = 0$ (zero-field shift of the EPR signal ($\Delta Z$)) was measured at different temperatures. Figure 6.6 shows the EPR spectra at $T = 370$ K, and Fig. 6.7 shows the plot of $\Delta Z$ versus temperature for the sample under consideration. The recorded EPR signal, which is the field derivative of the absorbed microwave power ($P = dP/dH$), depends on the sample magnetization state and on the local magnetic field at the nanoparticle position. The latter can be represented by the sum of the external magnetic field and the internal magnetic field ($H_{int}$), which is determined by sample magnetization. The internal field had opposite directions at the start and the end of the measurement procedure described above. Since the external field is equal to zero at these points, $\Delta Z$ can be presented as

$$P'(H_{int}(M_r)) - P'(-H_{int}(M_r)) \approx 2dP'/dH(0)H_{int}(M_r). (4)$$

If the shape of the EPR line does not change significantly with a change in temperature, it can be assumed that $\Delta Z \sim H_{int}(M_r) \sim TM_r$. Hence, using the thermal variation of $\Delta Z$, one can estimate the temperature dependence of remanent magnetization (Figs. 6.6, 6.7).

Below 100°C, $\Delta Z$ (and consequently, $M_r$) changes insignificantly. A noticeable decrease in $\Delta Z$ takes place above this temperature (Fig. 6.7). Extrapolation of the $\Delta Z(T)$ dependence to $\Delta Z = 0$ leads to the conclusion that $M_r$ disappears at about 160°C. Probably, the observed $M_r$ decrease can be associated with the softening of the polymeric matrix under heating. Nevertheless, one can conclude that the investigated material containing magnetic nanoparticles in a polymeric (PE) matrix has an ability to keep magnetization up to rather high temperatures.

To establish the character of $M_r$ changes with time, two measurements of the zero-field shift of the EPR signal for the plate sample with 5 wt % Fe in the PE matrix were made 12 h apart. It was found that the $\Delta Z$ value did not change within the error of the measure-

ment. This points to the long-term character of remanent magnetization in the samples.

To study the effect of the matrix on the properties of nanoparticles, EPR measurements were made for the sample containing 4.65 wt % Fe in the polyamide matrix (as is known, polyamide has a much more rigid structure than polyethylene and polypropylene). The EPR spectrum of the sample near room temperatures had a well-resolved powder-like character and some additional features in comparison with the PE matrix (Figs. 6.8, 6.9). The spectrum consisted of three resonance lines: the strongest central line and two weaker lines on the spectrum edges. Such a powder-like spectral pattern became more pronounced with an increase in temperature. The positions of the resonance lines were almost temperature independent. The low-field line corresponded to the resonance field $H_1 \approx 1700$ Oe; the high-field one, to $H_2 \approx 4200$ Oe. The "paramagnetic" value of the resonance field $H_0$ (central EPR line) was 3400 Oe, which corresponded to the effective $g$ value of about 2.08. On cooling the sample, the FMR spectra became simpler and contained only a single broad line, which was very temperature-sensitive below about 100 K (Fig. 6.9). At temperatures about 80 and 25 K, a sharp increase in linewidth $\Delta H$ was observed. The observed additional EPR lines (at $H_1$ and $H_2$) can be attributed to the effect of the $\alpha$-Fe-like magnetic anisotropy of particles. Analogous EPR spectra were simulated in [34] for a system of magnetic single-domain particles with uniaxial or cubic anisotropy. However, the calculations in [34] suggested a significant simplifying of EPR spectra with an increase in temperature, which was not observed in our case. This may be connected with the high blocking temperature of our sample.

### 6.2. Ni-Based Samples

The EPR spectra for the sample containing 1 wt % Ni in the PE matrix exhibit a common superparamagnetic behavior analogous to that found for Fe-based samples. The room-temperature spectrum consists of a single symmetric line with $g \approx 2$ and the line width $\Delta H \approx 500$ Oe. As temperature rises, the line is slightly narrowed (to 380 Oe at 470 K). Sample cooling resulted in a broadening of the line (up to 1 kOe at 110 K), the line shape being roughly unaltered.

### 6.3. Ferrite Ba-Based Samples

Three types of samples containing Ba oxide nanoparticles––$BaFe_2O_4$ and $BaFe_{12}O_{19}$ (5 wt %) in the PE matrix––were studied by EPR. For $BaFe_2O_4$ samples, the broad line predominates in the room-temperature spectra with parameters analogous to that observed for the sample with 5 wt % $Fe_2O_3$ in the PE matrix. In the room-temperature spectrum of the $BaFe_{12}O_{19}$ sample,
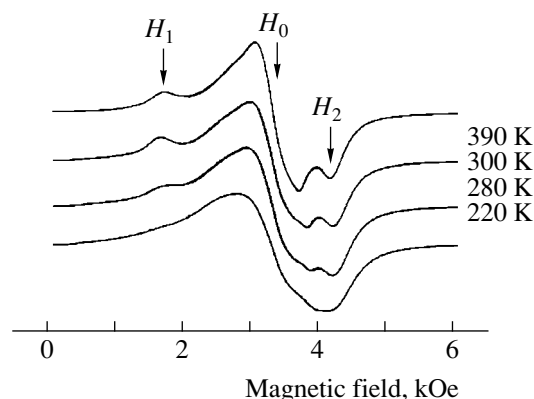


**Fig. 6.8.** FMR spectra for the sample containing 4.65 wt % Fe in the polyamide matrix in a high-temperature region.
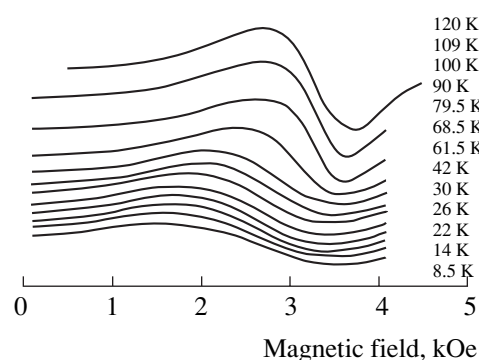


**Fig. 6.9.** FMR spectra for the sample containing 4.65 wt % Fe in polyamide matrix in a low-temperature region.

on the contrary, the narrow line with $\Delta H \approx 120$ Oe and $g \approx 2.00$ is more pronounced (Fig. 6.4).

The EPR spectra of the $BaFe_2O_4$ sample were broad and rather asymmetric at all temperatures. Below about 125 K the linewidth and the amplitude rapidly increased and decreased, respectively. Temperature dependences of $\Delta H$ and $A$ also reveal an additional anomaly near 50 K. As is known, bulk $BaFe_2O_4$ is nonmagnetic [35]. The observed strong EPR signal with a superparamagnetic character allows one to think that it is related to a phase with a radically different composition. The EPR spectrum behavior below 125 K suggests that such a phase could be magnetic $Fe_3O_4$, which undergoes the Verwey transition at 119 K [35]. It should be noted that the observed temperature behavior of the EPR linewidth in $BaFe_2O_4$ nanoparticles closely resembles that of commercially available nanoparticle material nanocat™ [36]. There is evidence that the major phase in nanocat is $Fe_3O_4$ [36]. The dependence $\Delta H(T)$ for nanocat shows similar features near 120 K and below 50 K as those observed in our $BaFe_2O_4$ sample. The acceleration of the EPR linewidth broadening below 50 K can be due to spin-glass freezing phenomena and has often been observed in various iron oxide nanoparticles [25, 28, 32].

EPR spectra of the $BaFe_{12}O_{19}$ sample at different temperatures showed a characteristic superparamagnetic behavior with an increase in the broad and a decrease in the narrow resonance under cooling. In contrast to the $BaFe_2O_4$ sample, the position of the broad line does not shift so significantly toward lower fields. Below 10 K, a fine structure was observed in the spectra at $g \approx 2$. The observed significant superparamagnetic narrowing of the EPR signal in the $BaFe_{12}O_{19}$ sample at high temperatures can be evidence of the reduced magnetic anisotropy. According to the literature data, bulk hexaferrite $BaFe_{12}O_{19}$ is characterized by high uniaxial anisotropy (about $3.3 \times 10^6$ erg/cm$^3$) [35]. Because, in nanoparticles, the contribution of the particle surface to the total magnetic anisotropy can be appreciable and can even dominate [29, 37], the high bulk anisotropy does not guarantee a high value of the anisotropy for nanoparticles. The reduction of anisotropy in nanoparticles can also be due to structural imperfections and/or to the particle smallness. Earlier, it was found that for $BaFe_{12}O_{19}$ nanoparticles with an effective diameter of less than approximately 12 nm, the specific magnetization and coercivity drastically decreased [38].

## 7. MAGNETIC STUDIES

From the magnetic standpoint, the materials under investigation can be regarded as the systems of noninteracting single-domain magnetic particles displaying superparamagnetic properties. The magnetic behavior of such systems can be described by the Stoner–Wohlfarth model [39], according to which the energy of a particle in the magnetic field can be expressed as

$$E = KV\sin^2\theta - \mu H\cos(\theta - \psi), \qquad (5)$$

where $K$ is the particle uniaxial anisotropy constant; $V$ is the particle volume; $\mu = VM_s$ is the magnetic moment of the particle with the saturation magnetization $M_s$; and $\theta$ and $\psi$ are the angles between the particle easy axis and its magnetic moment and between the applied field $H$ and the particle magnetic moment, respectively. It can be shown that for fields lower than a characteristic field $H_k = 2K/M_s$ (the anisotropy field), two minima of the energy function $E$ exist, separated by the field-dependent energy barrier $E_b$. These two minima correspond to the opposite orientations of the particle magnetic moment. The energy barrier in the presence of the magnetic field $H$ is given by

$$E_b = KV(1 - H/H_k)^2. \qquad (6)$$

In the course of magnetization, once the magnetic field has reached the value of $H = H_k$, the magnetization reversal occurs. In the Stoner–Wohlfarth model, it is supposed that coherent spin rotation takes place; i.e., all spins during magnetization reversal remain parallel. The magnetization curve $M(H)$ of the system can be calculated numerically using Eq. (5). The anisotropic

properties of the particle lead to the appearance of hysteretic properties, with a characteristic hysteresis loop in the $M(H)$ curve. The magnetic anisotropy of the particle can result from the magnetocrystalline anisotropy of its material, shape anisotropy, strain anisotropy, and the surface anisotropy related with the breaking of the symmetry at the surface and the interaction between the particle and its surrounding material.

At a finite temperature, the particle magnetic moments can overcome the energy barrier $E_b$ by means of thermal agitation. The relaxation time $\tau_r$ for this process can be described by the Neel–Arrhenius law [20]:

$$\tau_r = \tau_0\exp(KV/k_BT), \qquad (7)$$

where $\tau_0$ is the constant on the order of $10^{-9}$ s. In the case of $H = 0$, $E_b = KV$ and the relaxation process is essentially determined by the particle anisotropy and volume.

If a time characteristic of the measurement process ($\tau$) is much larger than $\tau_r$, the particle magnetic moments can relax freely leading to a thermal equilibrium behavior without any hysteresis. In contrast, if $\tau_r > \tau$, the particles are thermally stable and the system exhibits an irreversible magnetic behavior with hysteretic properties. Using the value $\tau = 10^2$ s characteristic for quasi-static magnetic measurements gives (in the case of $H = 0$) the Bean–Livingstone relation for the magnetic blocking temperature $T_b^m$ [40]:

$$T_b^m = KV/25k_B. \qquad (8)$$

$T_b^m$ marks the transition to the so-called blocking state, which, in principle, can be treated as an analog of the magnetically ordered state in bulk materials. Below $T_b^m$, the system of magnetic anisotropic nanoparticles displays the hysteretic properties necessary for magnetic recording purposes. It is widely accepted to determine $T_b^m$ as the point at which temperature hysteresis in the ZFC–FC curves (see below) appears [41, 42].

From the Stoner–Wohlfarth energy barrier–field dependence (Eq. (6)), the following temperature dependence for the coercive force of the blocked superparamagnetic system was obtained:

$$H_c(T) = H_c(0)(1 - aT^{1/2}), \qquad (9)$$

where $H_c(0)$ is the value of the coercive force at $T = 0$ K and $a$ is a coefficient. Using the fact that the coercive force disappears above $T_b^m$, it is possible to obtain $T_b^m$ from the experimental $H_c(T)$ dependence as $T_b^m = 1/a^2$. Victoria [43] has shown that another than the Stoner–Wohlfarth field dependence of $E_b$ is possible: $E_b \sim H^{3/2}$, which gives the temperature dependence of $H_c(T)$ as $T^{2/3}$.

A magnetization isotherm $M(H)$ of a superparamagnet can be presented using the Langevin function as [44]

$$M = M_s L(H/k_B T), \qquad (10)$$

where $L(x) = \coth(x) - 1/x$ is the Langevin function, $M_s$ is the saturation magnetization, and $\mu$ is the magnetic moment of a particle.

Our X-ray, Mössbauer, and EPR studies showed that Fe nanoparticles include $\alpha$-Fe, iron oxides (mainly $\gamma$-$Fe_2O_3$ and $Fe_3O_4$), and various iron carbides. In the bulk form, all of them have high Curie temperatures well above room temperature: $\alpha$-Fe, 1043 K; $\gamma$-$Fe_2O_3$, 848 K; $Fe_3O_4$, 858 K; $Fe_3C$, 483 K; and $Fe_2C$, 653 or 520 K (depending on the crystal structure) [44, 45]. The Curie temperatures of Co and Ni are 1394 and 655 K, respectively [45]. The anisotropy constants are $4.78 \times 10^5$ erg/cm$^3$ for Fe, $4.0 \times 10^6$ erg/cm$^3$ for Co, and $-5.8 \times 10^4$ erg/cm$^3$ for Ni at room temperature [45]. Using these constants and Eq. (8), one can estimate the values of the particle diameters necessary to obtain the blocked state of the system at room temperature. They are about 16 nm for Fe, 8 nm for Co, and 34 nm for Ni. At the same time, it is necessary to note that the nanoparticle anisotropy can be much higher than that of the corresponding material in the bulk state. Thus, the real size of the nanoparticles blocked at room temperature can be much smaller than the values listed above.

For the magnetization temperature and the field dependences measurements, a Princeton Applied Research vibrating sample magnetometer (model PARC-155) equipped with a flow helium cryostat and a high temperature insert was used. The sensitivity of the magnetometer was better than $5 \times 10^{-5}$ emu. The magnetic measurements were carried out in the temperature range from 4.2 to 380 K and in magnetic fields up to 4.5 kOe. Measurements of hysteresis loops were made by saturating the pristine sample in a maximum available field of 4.5 kOe. From the loops, the coercive field ($H_c$) and the remanent magnetization $M_r$ were determined. To investigate the "blocking" properties of our materials, so-called field-cooled (FC) and zero-field-cooled (ZFC) magnetization measurements were made. In the ZFC measurement, the sample was cooled in the absence of magnetic field down to 4.2 K and, then, magnetization was measured while the sample was warmed in the desired field. In the FC measurement, the magnetization was measured while the sample was cooled in the presence of the desired field.

### 7.1. Fe-Based Samples

Magnetic properties of Fe nanoparticles were studied in [46–49]. Hou *et al.* [46] prepared a powder of Fe-based nanoparticles by reducing $Fe_3O_4$ nanoparticles coated with $SiO_2$ to avoid agglomeration. The median diameter of the particles was about 20 nm. The particles have a core–shell structure with the core con-

sisting of $\alpha$-Fe (major portion of the particle) and the shell consisting of iron oxide. The particles with different contents of iron oxide were prepared. It was established that the particles with the lowest oxide content were characterized by the highest magnetic anisotropy values (with anisotropy constant $K$ of about $1.42 \times 10^6$ erg/cm$^3$). Increasing the iron oxide content led to the decrease in magnetic anisotropy to $K = 7.8 \times 10^5$ erg/cm$^3$. The authors related this decrease with the lower magnetic anisotropy in iron oxide than in $\alpha$-Fe. Bodker *et al.* [47] established the magnetic anisotropy constant equal to $1.2 \times 10^6$ erg/cm$^3$ in carbon-supported $\alpha$-Fe nanoparticles with an average size of 3 nm from ac magnetic susceptibility measurements. Prados *et al.* [48] studied $\alpha$-Fe nanoparticles prepared by the inert gas condensation method with subsequent oxygen passivation. The nanoparticles have a core–shell structure with the iron oxide shell, and their diameters range from 2.5 to 10 nm, depending on preparation conditions. They displayed at 5 K a coercive force ($H_c$) of about 1300 Oe, which decreased with an increase in particle diameter. The authors explained the hysteretic properties of the particles by unidirectional anisotropy [27]. Santos *et al.* [49] studied Fe particles embedded in alumina ($Al_2O_3$) matrix. The samples contained 7.8 wt % Fe and various ratios of Fe and iron oxides depending on heat treatment conditions. According to magnetization measurements, samples containing 18% Fe (the rest was $Fe_3O_4$ and $\alpha$-$Fe_2O_3$ oxides) exhibited a coercive force of 819 Oe at 300 K and 1142 Oe at 80 K and a saturation magnetization of 2 emu/g at 300 K. The samples with a high $\alpha$-Fe content (about 70%) display $H_c = 370$ Oe and a saturation magnetization of 9 emu/g at 300 K.

In our work, magnetic measurements were made for Fe-based samples obtained in wide range of concentrations (up to 50 wt %), under various preparation conditions, with various polymeric matrices, and exposed to various kinds of treatment.

All investigated Fe samples exhibited hysteretic properties with coercive force $H_c$ depending on the Fe concentration and the preparation conditions. The maximum value of $H_c$ (950 Oe) was observed in the sample containing 5 wt % Fe in the PE matrix. Samples with the same composition prepared in different experiments had some scattering in $H_c$: for samples with 5 wt % Fe in the PE matrix, the scatter was about 300 Oe. The magnetic moment per Fe atom also depended on the Fe concentration, the type of polymeric matrix, and the preparation conditions, and for the samples with 5 wt % Fe had the value in the range of 0.7–1.0 $\mu_B$/atom in the field of 4.5 kOe at room temperature. Figure 7.1 shows a typical hysteresis loop measured at room temperature for a plate sample containing 5 wt % Fe in the PE matrix with $H_c = 950$ Oe. The major portion of the experimental results was obtained for the samples containing 5 wt % Fe in the PE matrix. Samples with other Fe contents in the PE matrixes were characterized by smaller
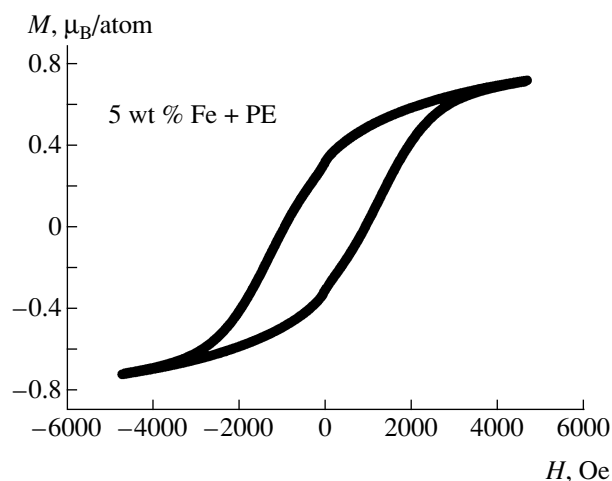
**Fig. 7.1.** Hysteresis loop of the plate sample containing 5 wt % Fe in the PE matrix measured at room temperature.
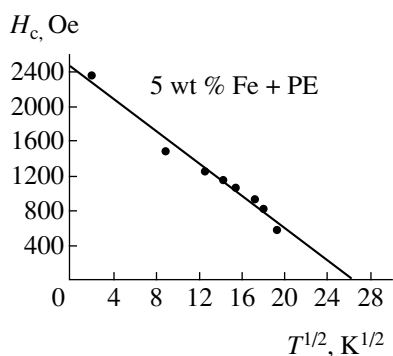


**Fig. 7.2.** Coercive force vs. $T^{1/2}$ for the plate sample containing 5 wt % Fe in the PE matrix. Data points correspond to experimental values, and the solid line is a least-squares approximation to Eq. (9).

values of the coercive force, with its decrease while the Fe content increased (for the samples with 30 and 50 wt % Fe, $H_c$ was 240 and 40 Oe, respectively).

Using polynomial interpolation, the initial magnetization curve was extracted from the hysteresis loop (Fig. 7.1) and then fitted by the Langevin function (10). The Langevin function fit gave the values of $M_s \approx 1 \ \mu_B$/atom and $\mu \approx 6000 \ \mu_B$. The $\mu$ value increased with an increase in the Fe content ($\mu \approx 1.8 \times 10^4 \ \mu_B$ for the

**Table 7.1.** Coercive force $H_c$ and remanent magnetization $M_r$ of a powder sample with 5 wt % Fe in the PE matrix after exposure to air for different periods of time

| Exposure time, h | $H_c$, % | $M_r$, % |
|---|---|---|
| Original | 100 | 100 |
| 24 | 99 | 98 |
| 120 | 97.7 | 95.2 |
| 336 | 94.1 | 92.6 |

sample with 10 wt % Fe in the PE matrix) that points to the increase in particle size. Remanent magnetization $M_r$ usually was about 1/3 of $M_s$ in almost all investigated Fe-based samples. ZFC–FC measurements made for the sample with 5 wt % Fe in the PE matrix showed that its blocking temperature is higher than room temperature.

The temperature dependence of the coercive force $H_c$ was measured for a plate sample with 5 wt % Fe in the PE matrix at temperatures up to 100°C. Heating the sample led to a decrease in $H_c$ and $M_r$. It should be noted, that after cooling back to room temperature, the magnetic properties of the sample were exactly the same as before heating. The $H_c(T)$ dependence obeys the $T^{1/2}$ law (Fig. 7.2), determined in the framework of the Stoner–Wohlfarth model (Eq. (9)). The experimental data fit to $T^{1/2}$ dependence gives $H_c = 2475$ Oe at 0 K, and the temperature at which $H_c$ vanishes is 670 K. Because there should be no hysteresis above the blocking temperature, this temperature could be regarded as the blocking temperature $T_b^m$. It should be noted, that according to the EPR data, $M_r$ disappears at about 430 K (see Fig. 6.7), which is consistent with the magnetization data.

Using Eq. (8), the experimental values of $T_b^m = 670$ K, and the average nanoparticle diameter 3.57 nm for the sample with 5 wt % Fe in the PE matrix, we estimated the average anisotropy constant for Fe nanoparticles to be about $9.5 \times 10^7$ erg/cm³. This is close to $5.9 \times 10^7$ erg/cm³ recently obtained for the annealed 4 nm $Fe_{48}Pt_{52}$ fct nanoparticles at the IBM Research Center [5].

Table 7.1 contains the hysteresis loop parameters of the powder sample with 5 wt % Fe in the PE matrix after keeping it in air at room temperature for different periods of time. As it can be seen, exposure to air for two weeks resulted in about a 7% decrease in $M_r$ and $H_c$. For the plate sample with the same composition, no changes in the hysteresis loop parameters were found after keeping the sample in air for one month. We also studied the time relaxation of $M_r$ for this sample at room temperature. The sample was previously magnetized in a field of 4.5 kOe. Then, magnetization measurements in zero magnetic fields after 1, 24, and 168 h were conducted. Our results (see Table 7.2) showed the 4% decrease in magnetization after 168 h.

A set of experiments were conducted to investigate the influence of the technological parameters of the sample preparation and sample heat treatment on the magnetic properties of the materials under investigation. The influence of the preparation conditions on the magnetic properties of the samples was studied for a set of powder samples with 1.3 and 5 wt % Fe in the PE matrix synthesized at 240°C by the reaction of pentacarbonyl thermodestruction. The sample preparation conditions differed from sample to sample in the man-

**Table 7.2.** Relaxation of magnetization of the plate sample containing 5 wt % Fe in the PE matrix

| Time, h | $M_r$, % |
|---------|----------|
| 1 | 100 |
| 24 | 97 |
| 168 | 96 |

ner of (1) adding pentacarbonyl to the reaction mixture (by drops or at once), (2) stirring the reaction mixture (with or without stirring), and (3) cooling the reaction mixture (in the presence or absence of the external magnetic field).

The obtained hysteresis loop parameters measured at room temperature are summarized in Table 7.3. It should be noted that subsequent measurements for samples with 5 wt % Fe in the PE matrix prepared in different external magnetic fields up to 3.3 kOe (other conditions being identical) showed a coercive force increase for the samples prepared in a stronger external field.

A set of samples containing 5 wt % Fe in the PE matrix was used to investigate how their magnetic properties depend on the technological treatment, such as rinsing (treatment with a solvent, benzene). Magnetization, Mössbauer, and EPR measurements were made on the following samples: (1) an as-prepared powder without rinsing, (2) an as-prepared powder rinsed for 3 h (partly rinsed sample), (4) an as-prepared sample rinsed for 12 h, and (5) a plate sample pressed from the powder rinsed for 12 h. Hysteresis loop measurement showed that $H_c$ was the same in all samples. At the same time, magnetization at 4.5 kOe did not change in the partly rinsed sample and increased roughly threefold after rinsing for 12 h. Pressing the plate did not lead to an essential increase in magnetization. In the Mössbauer spectra of the pristine sample, a sextet with relatively broad and low-amplitude components was not distinctly visible. After rinsing for 12 h, the sextet becomes sharply defined. This can be explained by an increase in the molecular field acting on the atomic nuclei due to the increase in sample mag-

netization. The latter is connected with an increase in the concentration of magnetic particles in the sample after removing the extant oil by rinsing. The EPR spectra of the samples can be represented by a superposition of wide and narrow lines. Rinsing for 12 h led to a change in the ratio of the narrow and broad components in favor of the former. Further narrowing was observed in the pressed plate sample. As was previously found for various nanoparticle systems, smaller particles and $\gamma$-$Fe_2O_3$ are characterized by a narrower EPR signal. The broad EPR signal arises from amorphous Fe. The observed changes in EPR spectra can be explained by some additional oxidation and washing out of larger nanoparticles and some recrystallization of amorphous Fe in the particles during pressing.

In further rinsing experiments, the as-prepared powder sample with 5 wt % Fe in the PE matrix was treated with benzene for 12, 24 and 36 h. After 12-h rinsing, the magnetization increased and the coercive force did not change. However, further rinsing led to a significant decrease in both $H_c$ and magnetization. $H_c$ completely vanished after rinsing for 24 h, and the magnetization was about 0.1 of its initial value with a paramagnetic-type $M(H)$ curve after 36 h of rinsing. We measured $M(H)$ dependences of the dried deposit formed in the solvent during rinsing. Its magnetization curves had a ferromagnetic character without hysteresis. This behavior can be related to the removal of particles from the sample during prolonged rinsing. The particles in the deposit are not fixed in a matrix and that is why they can be freely rotated by the magnetic field, which leads to the absence of the coercive force in the deposit. Therefore, it can be concluded that the fixation of particles in the matrix (and their interaction with the matrix) plays one of the dominant roles in forming the hysteretic properties of materials.

The sample containing 5 wt % Fe in the PE matrix prepared from iron formate $Fe(HCOO)_3$ by thermodestruction at 230°C did not reveal any hysteresis at room temperature. Its magnetization was low (0.025 $\mu_B$/atom in a field of 4.5 kOe) and had a superparamagnetic field dependence.

**Table 7.3.** Influence of the preparation conditions on the room temperature hysteretic parameters of powder Fe-containing samples with a PE matrix

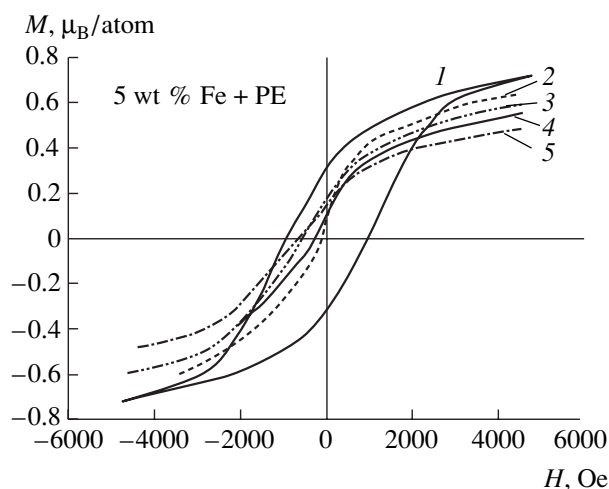| Sample | A | B | C | D | E | F |
|--------|-----|-----|-----|-----|-----|-----|
| Fe content, % | 5.0 | 5.0 | 5.0 | 1.3 | 1.3 | 1.3 |
| Coercivity $H_c$, Oe | 540 | 680 | 450 | 270 | 530 | 130 |
| Saturation magnetization $M_s$, $\mu_B$ per Fe atom | 1.1 | 0.90 | 0.78 | 0.64 | – | – |
| Remanent magnetization $M_r/M_s$ | 0.32 | 0.37 | 0.31 | 0.21 | 0.31 | 0.20 |
| Mixing of MCC | By drops | At once | By drops | At once | By drops | At once |
| Stirring | Yes | Yes | Yes | No | No | Yes |
| Magnetic field, kOe | No field | 3.3 | 2.8 | 3.3 | 3.3 | 1.1 |

**Fig. 7.3.** Room-temperature hysteresis loop for the original sample containing 5 wt % Fe in the PE matrix (curve *1*) and demagnetization curves for the sample heat treated in air at (*2*) 29, (*3*) 240, (*4*) 260, and (*5*) 195°C.



**Fig. 7.4.** ZFC–FC curves measured in 300 Oe for the (*1*, *2*) original and (*3*, *4*) heat-treated (at 280°C for 6 h) sample containing 5 wt % Fe in PE matrix: (*1*, *3*) FC and (*2*, *4*) ZFC.

We studied the influence of heat treatment on the magnetic properties of a sample containing 5 wt % Fe in the PE matrix at temperatures of 195, 215, 240, 260 and 290°C in air. For each temperature, we took two pieces of the sample. We held both pieces at the desired temperature for 10 min. Then, one piece was placed in the magnetic field of 7 kOe (texturing magnetic field). For the samples cooled in magnetic field, we measured the magnetization curves along and transversely to the direction of the texturing magnetic field. We did not find any differences between these curves and the magnetization curves of the samples cooled without external magnetic field for all temperatures of heat treatment. Such a behavior can reflect the presence of strong chemical bonding of metallic particles with the surrounding polymeric matrix and a small contribution of the shape magnetic anisotropy to the total anisotropy of the particles.

**Table 7.4.** Remanent magnetization $M_r$, coercive force $H_c$, and magnetization at 4.5 kOe at room temperature and at 100°C for the samples containing 5 wt % Fe heat treated at different temperatures in air

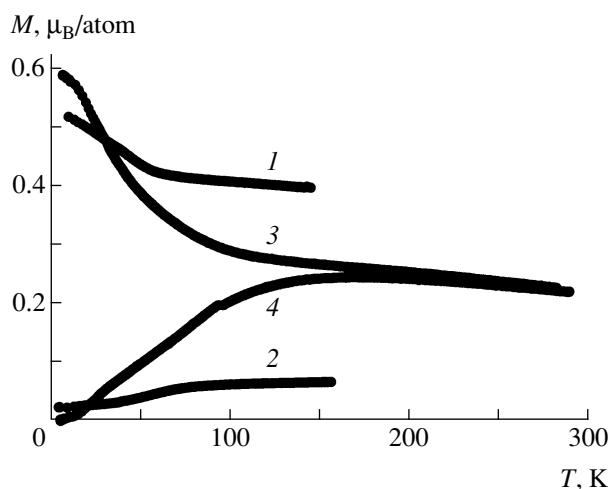|  | $H_c$ | $M_r$ | $M$ (at 4.5 kOe) | $H_c$ (at 100°C) |
|---|---|---|---|---|
|  | Oe | $\mu_B$ | $\mu_B$ | Oe |
| Original | 950 | 0.25 | 0.72 | 566 |
| 195°C | 720 | 0.16 | 0.48 | |
| 215°C | 570 | 0.14 | 0.50 | |
| 240°C | 490 | 0.15 | 0.56 | |
| 260°C | 270 | 0.10 | 0.55 | 230 |
| 290°C | 170 | 0.08 | 0.64 | |

The magnetization curves of the samples heat treated at different temperatures are shown in Fig. 7.3. The corresponding values of the remanent magnetization, magnetization in the field of 4.5 kOe, and coercive force measured at room temperature and at 100°C are summarized in Table 7.4.

As one can see, heat treatment leads to a progressive decrease in the coercive force of the samples. The fastest coercive force decrease is observed in the temperature range 240–260°C, i.e., in the range of polyethylene melting. It was determined from Mössbauer spectra that heating causes an increase in the iron oxide content (see Section 5). That is why the decrease in the coercive force can be related to the particle oxidation (it should be noted that $\gamma$-Fe$_2$O$_3$ has a significantly lower magnetocrystalline anisotropy than pure Fe).

The behavior of the specific magnetization is more complex. Whereas the remanent magnetization consistently decreases with an increase in the heat treatment temperature, which simply reflects the decrease in the sample coercive force, the magnetization in the field of 4.5 kOe first markedly decreases and then increases (see Table 7.4). The observed magnetization decrease can also be related to the oxidation of nanoparticles. According to the Mössbauer measurements for the samples with the same composition heat treated in an analogous manner, previously formed iron(III) oxide is reduced to the oxide containing Fe$^{+2.5}$ at high temperatures of treatment. This process can be responsible for the magnetization increase in the samples heat treated at high temperatures.

Hysteresis loops were measured for the sample heat treated at 210°C for 10 and 60 min. The increase in heat treatment time led to a further decrease in $H_c$ by about 5%, which can be associated with further oxidation. The blocking temperature also decreased after high-

temperature heat treatment. Figure 7.4 shows the ZFC–FC curves for the original (not heat treated) and heat-treated (6 h at 280°C) sample containing 5 wt % Fe in the PE matrix. The magnetization temperature hysteresis characteristic for the blocking state becomes visible for the heat-treated sample at about 250 K (it follows from $H_c(T)$ measurements that the blocking temperature for the original sample is about 670 K). Rapid magnetization rising below 70 K can be related to the transformations of the particle internal magnetic structure.

We also measured the coercive force in the samples containing 5 wt % Fe in the PE matrix (with the coercive force of 950 Oe) after exposing them to –70°C and the liquid-nitrogen temperature for various periods of time and cycling between –70 and +30°C. The samples were kept at –70°C for up to 9 h and at the liquid-nitrogen temperature for up to 21 h. On cycling, the samples were cooled down to –70°C and kept at this temperature up to 2 h; then, they were heated up to +30°C and kept at this temperature for 30 min. Five cooling–heating cycles were made. This treatment did not lead to a noticeable change in the coercive force: its difference from the initial value was in the range of 30–50 Oe.

Figure 7.5 shows the room-temperature magnetization curves of a commercially available micron-sized carbonyl Fe powder and two samples containing 5 and 12.3 wt % of micron-sized Fe particles in the PE matrix. The latter samples were prepared by simply adding the Fe micron-sized powder to the melt of polyethylene in mineral oil. The coercive force was equal to zero in all three samples. The magnetization curves were not saturated due to the effects of the demagnetization fields inside the particles. The specific magnetization of the Fe powder approached the value of 2.2 $\mu_B$/atom. The specific magnetization of the samples containing micron-sized particles in the PE matrix was about half as large as that of the pure Fe powder. This can be related with Fe losses on the stage of rinsing. Fe loss arises due to the weak bonding of micron-sized particles to the polymeric matrix in the resulting composite materials. These samples can be regarded as a simple mechanical mixture of two separate phases, a polymer and Fe particles. On the contrary, the magnetic
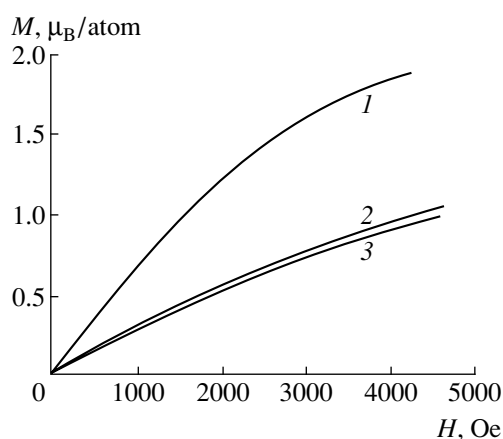


**Fig. 7.5.** Room-temperature magnetization curves for micron-sized Fe powder (curve *1*) and for the samples containing 5 (curve *3*) and 12.3 wt % (curve *2*) of micron-sized Fe particles in the PE matrix.

polymers containing nanoparticles studied in this work are characterized by essential particle binding to the surrounding polymeric matrix.

The results of studying the powder samples containing various amounts of Fe in the PP and PAMD matrices are summarized in Tables 7.5 and 7.6. In the samples with PAMD and PP matrices, the coercive force increases with increasing the Fe concentration. However, the room-temperature values of $H_c$ in these samples were at least three times lower than in the samples containing 5 wt % Fe in the PE matrix. Heat treatment of the samples at 300°C for 10 min led to a decrease in the coercive force and to an increase in the specific magnetization.

We studied the influence of matrix rigidity on the magnetic properties of Fe-based samples. To do this, the following samples were prepared: 5 wt % Fe in the paraffin matrix and 30 wt % Fe (relative to PE) in a mixed PE–paraffin matrix. In the latter case, the relative content of polyethylene in more rigid paraffin was successively increased: the samples with 5, 10 and 20 wt % PE (relative to paraffin) were prepared. The sample with 5 wt % Fe in the paraffin matrix had a coercive force of

**Table 7.5.** Coercive force $H_c$, remanent magnetization $M_r$, magnetization in the field of 4.5 kOe for powder samples containing Fe in polyethylene and polyamide matrices

| Matrix | Fe, % | Room temperature | | | $T = 77$ K | | |
|---|---|---|---|---|---|---|---|
| | | $H_c$ | $M_r$ | $M$ at 4.5 kOe | $H_c$ | $M_r$ | $M$ at 4.5 kOe |
| | | Oe | $\mu_B$ | $\mu_B$ | Oe | $\mu_B$ | $\mu_B$ |
| PP | 19.69 | 250 | 0.12 | 0.47 | | | |
| PP | 30 | 360 | 0.008 | 0.04 | 500 | 0.012 | 0.05 |
| PAMD | 5.2 | 110 | 0.096 | 0.59 | | | |
| PAMD | 14.2 | 180 | 0.09 | 0.49 | | | |
| PAMD | 48.2 | 340 | 0.18 | 0.71 | | | |

**Table 7.6.** Coercive force $H_c$, remanent magnetization $M_r$, magnetization in the field of 4.5 kOe at room temperature and at 100°C for the original powder samples containing Fe in polyethylene and polyamide matrices and the samples heat treated at 300°C for 10 min

|  | $H_c$ | $M_r$ | $M_{H=4.5}$ | $H_c$ (at 100°C) |
|---|---|---|---|---|
|  | Oe | $\mu_B$ | $\mu_B$ | Oe |
| 19.69% Fe in PP original | 250 | 0.12 | 0.47 | 180 |
| 19.69% Fe in PP heat treated | 120 | 0.06 | 0.65 | 100 |
| 5.2% Fe in PAMD original | 110 | 0.096 | 0.59 | 70 |
| 5.2% Fe in PAMD heat treated | 80 | 0.17 | 0.89 | 50 |
| 14.24% Fe in PAMD original | 180 | 0.09 | 0.49 | 120 |
| 14.24% Fe in PAMD heat treated | 80 | 0.06 | 0.65 | 50 |

about 650 Oe and a magnetization of 1.5 $\mu_B$/atom in the field of 4.5 kOe. In the set of samples containing 30 wt % Fe (relative to PE), the magnetization decreased from ~1 to ~0.3 $\mu_B$/atom with the increase in the PE content from 5 and 20 wt % PE. Simultaneously, the increase in the coercive force from about 100 Oe to about 900 Oe was observed.

## 7.2. Co-Based Samples

Magnetic properties of Co particles have been well documented [50–58, 60–67]. Woods *et al.* [50] studied thin films containing 5–10 layers of Co nanoparticles deposited on a thermally oxidized silicon substrate. Monodisperse Co nanoparticles were obtained by high-temperature solution phase synthesis. Each particle was coated by an oleic acid shell 2 nm in thickness. The particles were 3 and 5 nm in diameter and were assembled into closely-packed arrays with a spacing between particles of about 4 nm. The measurements of magnetic noise power density produced by the samples were made using a variable-temperature scanning SQUID microscope. From the data obtained, the blocking temperatures of 20 K and 55 K and the magnetic anisotropy constants of $3.08 \times 10^6$ and $1.87 \times 10^6$ erg/cm$^3$ were determined for the samples with 3- and 5-nm Co particles, respectively. Chen *et al.* [51] studied the magnetic behavior of Co nanoparticles synthesized in inversed micelles. The average diameter of the particles was 1.8–4.4 nm depending on preparation conditions. The blocking temperatures varied from 19 K for 1.8-nm particles to 50 K for 4.4-nm particles. The coercive force also increased with an increase in nanoparticle diameter ($H_c$ = 640 Oe for 1.8 nm and $H_c$ = 12.5 kOe for 4.4 nm at 10 K). The magnetic anisotropy constant determined from the blocking temperature was $3 \times 10^7$ and $5 \times 10^6$ erg/cm$^3$ for the particles with a diameter of 1.8 and 4.4 nm, respectively. The saturation magnetization for 1.8-nm particles was about 200 emu/g (2.1 $\mu_B$/atom), which is about 20% larger than the bulk value (162.5 emu/g or 1.7 $\mu_B$/atom [45]). Colloids containing cobalt nanoparticles were prepared by decomposition of an organometallic precursor in the presence of a stabilizing polymer by Respaud *et al.* [52, 53]. Two compositions with average particle diameters of 1.5 and 2.0 nm were obtained. The first one had a blocking temperature of 9 K; the second one, of 13.5 K. Magnetization measurements in high fields (up to 50 kOe) revealed deviations from the Langevin behavior in a superparamagnetic temperature region. From the magnetization measurements (fitting $M(H)$ curve to the Langevin function and taking into account the magnetic anisotropy of the particles), the magnetic anisotropy constants were determined to be $(0.83–1.3) \times 10^7$ and $(7.3–8.5) \times 10^6$ erg/cm$^3$ for the samples with a particle diameter of 1.5 and 2 nm, respectively. It was also found that the magnetization did not saturate even in high magnetic fields and the high-field susceptibility increased with reduction of the particle size. This behavior was related to a two-step magnetization process: orientation of the magnetic moments of the particles and orientation of the internal canted spin structure of the particle along the external magnetic field (this process contributes to the large high-field susceptibility). The magnetic moment per Co atom was found to be 1.94 and 1.83 $\mu_B$ for particles with diameters of 1.5 and 2 nm, respectively.

Peng *et al.* [54] obtained Co particle assemblies on a polyimide film with a thickness of about 100 nm using a plasma-gas-condensation type cluster beam deposition technique. The process was conducted in an argon atmosphere with oxygen admixture. The resulting particles had a mean diameter of 6 and 13 nm and a core–shell structure. The electron diffraction patterns showed the coexistence of fcc Co (core) and CoO (shell). Magnetization measurements revealed a field hysteretic behavior below about 200 K with a coercive force of about 2.5 kOe for 13-nm particles at 5 K. Below 200 K, the temperature ZFC–FC hysteresis was also observed. FC hysteresis loops displayed a bias characteristic for unidirectional exchange anisotropy below 200 K (for the sample with 6-nm nanoparticles, the bias was about 10.2 kOe after cooling in 20 kOe). The observed hysteretic behavior was explained by

uniaxial magnetic anisotropy related to exchange anisotropy [27]. The temperature at which the bias disappeared (~200 K), which marks an anisotropic exchange loss, was much lower than the Neel temperature of bulk CoO (293 K). Because of this observation, the authors suggested the exchange interaction between the ferromagnetic Co core and the disordered spins of the ferromagnetic–antiferromagnetic interface (Co–CoO) to be the main origin of exchange anisotropy. The spin glass freezing temperature of this noncollinear magnetically ordered layer was supposed to be 200 K. The unidirectional exchange anisotropy was also observed in oxide-passivated Co nanoparticles by Gangopadhyay et al. [55].

The magnetic properties of Co nanoparticles embedded in various matrices have been studied in [57, 58]. Dupuis et al. [56] studied Co nanoparticles with a diameter of 2.8 nm in conducting (Ag) and isolating (SiO$_x$) matrices. The samples were obtained using low-energy cluster beam deposition. Magnetization measurements showed that the blocking temperature increased from about 20 K for the samples with 5 at. % Co to about 70 K for the samples with 20 at. % Co. The difference between $T_b$ in Ag and SiO$_x$ matrices was insufficient. Jamet et al. [57] studied a system of Co nanoparticles with a diameter of 3 nm embedded in a 20-nm-thick Nb film. Samples were prepared by low-energy cluster beam deposition. The system of particles had a blocking temperature of 14 K and a magnetic anisotropy constant of $2 \times 10^6$ erg/cm$^3$. The contributions of the shape, magnetoelastic, magnetocrystalline, and surface anisotropy energies were considered to be possible sources of the observed magnetic anisotropy. It was shown that the main contribution arose from the surface anisotropy and could be explained in the framework of the Néel anisotropy model [59] by a breaking of the cubic symmetry at the particle surface. Hickey et al. [58] obtained small Co particles (less than 1.5 nm in diameter) in the Cu matrix by a rapid quenching of the molten Co$_{13}$Cu$_{87}$ alloy. The magnetic anisotropy of $3 \times 10^8$ erg/cm$^3$ was obtained for the particles containing 30 atoms of Co.

We measured the $M(H)$ curves for the samples containing 4–15 wt % Co in the PE matrix prepared under different conditions. Figure 7.6 shows the magnetization curves of the powder sample containing 4 wt % Co in the PE matrix synthesized at 300°C, measured at different temperatures. The observed field hysteresis points to the blocking state of the Co nanoparticle system at room temperature and below it. On cooling, the coercive force rises reaching 680 Oe at 4.2 K (at room temperature, it is 590 Oe). The magnetization also increases on cooling, although it is slightly temperature dependent below room temperature, in particular, in the region of 50 K where a Fe sample is characterized by a sharp magnetization rise with cooling (Fig. 7.7). Simultaneously, the character of the $M(H)$ dependence is changed: at room temperature, magnetization at 4.5 kOe approached the saturation value, while at
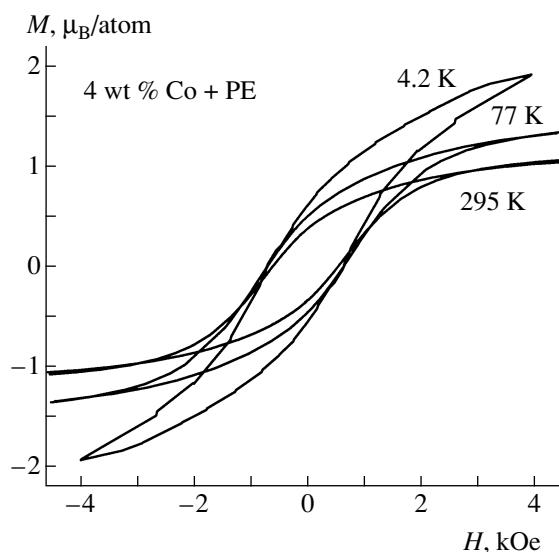


**Fig. 7.6.** Magnetization curves of the powder sample containing 4 wt % Co in the PE matrix prepared at 300°C.
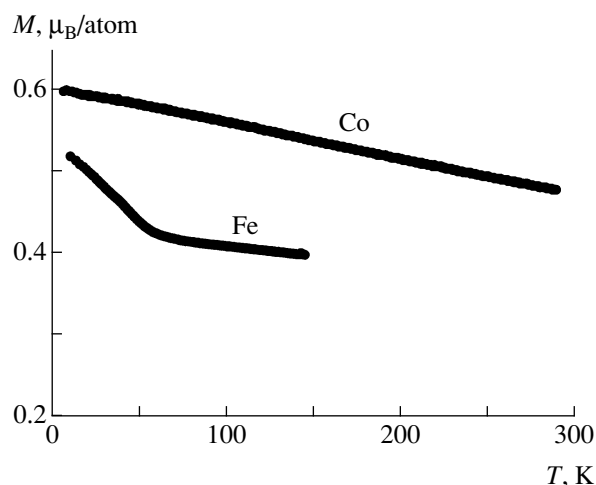


**Fig. 7.7.** FC (300 Oe) magnetization vs. temperature for Co and Fe samples with 4 and 5 wt % of the metal in the PE matrix, respectively.

4.2 K, saturation was absent. Such a behavior can be caused by an increase in the magnetic anisotropy in a low-temperature region. The magnetization at 4.5 kOe is 1.05 $\mu_B$/atom at 295 K and 1.95 $\mu_B$/atom at 4.2 K; the latter is greater than the volume value 1.7 $\mu_B$/atom [45]. Note that, according to elemental analysis, the oxygen content of the 4 wt % Co sample is no more than 0.04%. Theoretical calculations made in [60–64] predict the increase in magnetic moments in nanoparticles of 3$d$ transition metals Fe, Co, and Ni compared to the bulk values. This increase was related to a narrowing of the 3$d$ band in the surface layer of the particle due to a reduced coordination number of a 3$d$ atom at the surface. This effect is especially pronounced in small particles where the relative number of atoms at the surface is high and they play an essential role in the formation
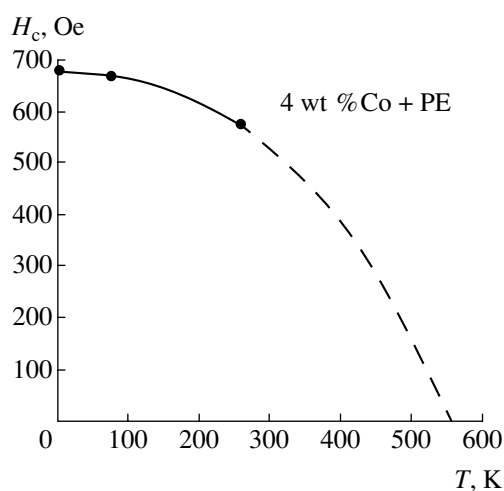
**Fig. 7.8.** Coercive force vs. temperature of the sample containing 4 wt % Co in the PE matrix prepared at 300°C.
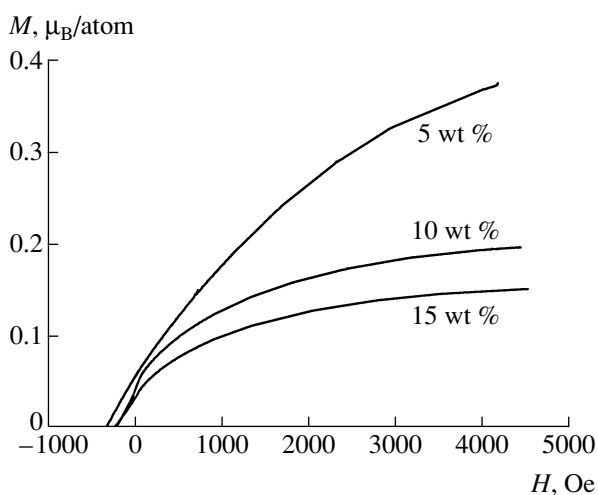


**Fig. 7.9.** Room-temperature demagnetization curves for the samples containing 5, 10, and 15 wt % Co in the PE matrix synthesized at 240°C and heat treated at 280°C for 6 h in air.

of the particle magnetic properties. The increase in the magnetic moment was observed experimentally in Co particles with a diameter of 1–2.5 nm in colloid (1.83–1.94 $\mu_B$/atom) [52, 53], 1.8–4-nm Co particles in micelles [51], and in the experiments with Fe, Co, and

**Table 7.7.** Coercive force $H_c$, remanent magnetization $M_r$, magnetization in the field of 4.5 kOe at room temperature for the original and heat-treated (280°C, 2 h) powder samples containing 4 wt % Co in the polyethylene matrix

|  | $H_c$ | $M_r$ | $M_{H=4.5}$ |
|---|---|---|---|
|  | Oe | $\mu_B$ | $\mu_B$ |
| 4 wt % Co in PE original | 590 | 0.35 | 1.05 |
| 4 wt % Co in PE heat treated | 590 | 0.62 | 1.96 |

Ni superparamagnetic clusters in molecular beams [63, 65–67]. In [66, 67], it was established that the Co magnetic moment in cluster is 2.2 $\mu_B$/atom.

The blocking temperature $T_b^m$ of the sample containing 4 wt % Co in the PE matrix can be determined from the $H_c(T)$ dependence. However, it was found that in contrast to the sample with 5 wt % Fe in the PE matrix, $H_c$ in the Co sample did not obey the $T^{1/2}$ law and fitting the experimental data to this law gave unrealistic $T_b^m$ values. The $T^2$ law gave the best fit to the data. Figure 7.8 shows the experimental $H_c$ values together with the approximating $T^2$ curve. Extrapolation of $T^2$ dependence to a high-temperature region allowed one to obtain the temperature at which the hysteresis disappeared (560 K), which can be regarded as $T_b^m$. By using this value and Eq. (8) (the particle diameter is 3 nm), one can estimate the effective anisotropy constant $K$ to be $1.5 \times 10^8$ erg/cm³, which is about two orders of magnitude higher than in bulk Co ($4 \times 10^6$ erg/cm³ at room temperature [45]).

The sample containing 4 wt % Co in the PE matrix was heat treated in air at 280°C for 2 h. The results of the heat treatment are shown in Table 7.7. As one can see, heat treatment does not change the coercive force of the sample. This can be related to an insufficient Co oxidation during heat treatment. Magnetization in the heat-treated sample was about twice as large as in the original sample. This increase can be connected with processes of crystal structure transformations in Co nanoparticles. Heat treatment and high-temperature magnetization measurements of the Co sample reveal an essential difference in the coercive behavior between this sample and the Fe sample of analogous composition. In the latter, heat treatment led to the decrease in both $H_c$ and magnetization (Table 7.4).

From the standpoint of the results obtained for the Co sample synthesized at 300°C, one could expect that increasing the temperature of synthesis could give the samples with better magnetic characteristics (in particular, higher magnetization). The increase in the preparation temperature could lead to a more complete particle formation but also to the formation of too large particles. A possible solution is a two-stage preparation process. At the first stage, we obtain samples with small Co particles by conducting the process at a lower temperature (240°C). At the second recrystallization stage (heat treatment at higher temperatures), larger nanoparticles form from tiny Co clusters. At this stage, the high viscosity of the polymer prevents the formation of too large particles.

A series of samples containing Co in the PE matrix with the metal concentrations 5, 10, and 15 wt % was synthesized at 240°C. The highest $H_c$ value of about 400 Oe was observed in the sample with 5 wt % Co. The as-prepared samples were characterized by small

magnetization (the highest value in 4.5 kOe was 0.016 $\mu_B$/atom). Heat treatment in air at 280°C for 6 h led to a roughly 30-fold increase in magnetization. The coercive force did not change. Figure 7.9 shows the room-temperature demagnetization curves for the samples containing 5, 10, and 15 wt % Co in the PE matrix synthesized at 240°C and heat treated at 280°C for 6 h in air.

### 7.3. Heterometallic Particles

Magnetic properties of heterometallic nanoparticles have been studied in [68–71]. Li *et al.* [68] obtained heterometallic $Fe_{1-x}Co_x$ nanoparticles with Co concentration $x = 0$, 0.2, 0.4, 0.6, 0.8, and 1 using the hydrogen plasma-metal reaction method. As-prepared particles had mean diameters from 40 to 51 nm and an oxygen content no more than 2.5 wt % depending on composition. The crystalline phase content, lattice constants, and magnetic characteristics of the nanoparticles displayed the same dependence on composition as those of the corresponding bulk alloys. In particular, there was a maximum of about 180 emu/g in the saturation magnetization–composition dependence at 40% Co (in the bulk, the $M_s$ maximum value is 240 emu/g). The coercive force in the nanoparticle system had a maximum value of 860 Oe at $x = 0.8$. $H_c$ increased with Co concentration increasing from about zero for pure Fe nanoparticles. The sample oxidized at 873 K in air was composed of $\alpha$-$Fe_2O_3$, $CoFe_2O_4$, and $Co_3O_4$ and had an acicular shape being 1000 nm in length and 30 nm in width. The magnetic properties of the oxidized nanoparticles were determined by $CoFe_2O_4$. The coercive force of the oxidized particles was 1 kOe higher in the whole composition range. Turgut *et al.* [69] studied the powder of oxide-coated FeCo nanoparticles prepared in an rf plasma torch reactor. The particles had an average diameter of 27 nm and contained $\alpha$-FeCo phase and $CoFe_2O_4$. The coercive force at 250 K was found to be about 140 Oe and the room-temperature magnetization was 190 emu/g. On cooling, $H_c$ rose up to 280 Oe at 5 K. Exchange anisotropy effects were observed (shifted hysteresis loops), which resulted from the interaction between the ferromagnetic FeCo core and the ferromagnetic $CoFe_2O_4$ shell.

The magnetization measurements of PdFe nanoparticles (Pd–0.4 at. % Fe) were made by Shinohara *et al.* [70]. The nanoparticles of various diameter (from 8.2 to 34.4 nm) were produced by the gas evaporation method in an Ar atmosphere. It was established that the spontaneous magnetization of the particles decreased with a decrease in the particle size. The results were explained in terms of the core–shell model by the existence of a nonmagnetic layer on the particle surface. The thickness of the layer was estimated from the experimental magnetization data to be about 3.3 nm. The core magnetization was comparable with the bulk value of 2.1 emu/g. The nature of the surface nonmagnetic layer
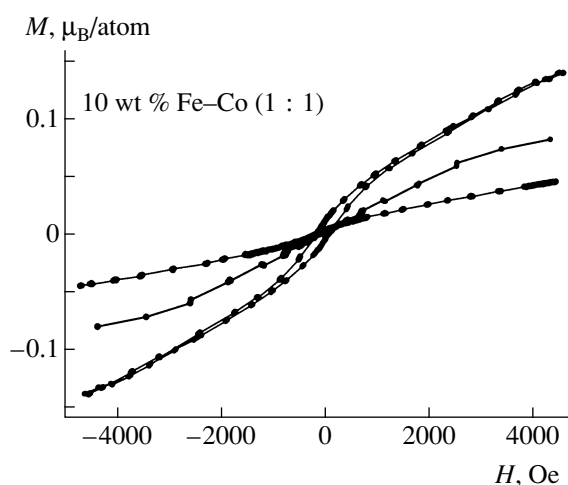


**Fig. 7.10.** Magnetization curves for the sample containing 10 wt % Fe–Co (1 : 1) in the PE matrix measured at 4.2, 77, and 295 K.

was related with localization of electrons in the layer. This localization decreases the itinerancy of electrons, which determines the magnetism of the material.

Chowdary *et al.* [71] prepared $SmCo_5$ nanoparticles with an average diameter of 40 nm by ball milling. It was found that their coercive force decreased with reduction of the strain imparted to the particle in the course of the preparation process.

In this work, we studied the following heterometallic powder samples: 10 wt % Fe–Pt (with a 1 : 1 metal-to-metal ratio), 5.5 wt % Fe–Co (10 : 1), 6 wt % Fe–Co (5 : 1), 10 wt % Fe–Co (1 : 1), and 6.5 wt % Fe–Sm (3 : 1) in the PE matrix.

The Fe–Pt sample exhibited at room temperature pure paramagnetic behavior with a linear $M(H)$ plot. The magnetization at 4.5 kOe was 0.3 $\mu_B$ per average magnetic atom.

The sample containing 5.5 wt % Fe–Co was prepared by the simultaneous thermodestruction of Co and Fe formates ($Co(HCOO)_2$ and $Fe(HCOO)_2$) at 250°C. It was characterized by paramagnetic behavior at room temperature with a magnetization of 0.025 $\mu_B$/magnetic atom in 4.5 kOe. The sample containing 10 wt % Fe–Co was synthesized by the thermodestruction of the $FeCo(CO)_4$ cluster at 300°C. It also revealed a paramagnetic magnetization curve at room temperature with a slightly higher magnetization of about 0.04 $\mu_B$/magnetic atom in the field of 4.5 kOe. The magnetization curves for this sample are shown in Fig. 7.10. On cooling, the magnetization increased and a small hysteresis of about 100 Oe appeared at 4.2 K. The $M(H)$ curve did not saturate in 4.5 kOe even at 4.2 K. The difference between the ZFC and FC magnetization curves (temperature hysteresis) (Fig. 7.11) appeared only below 25 K, which can be considered to be the blocking temperature.
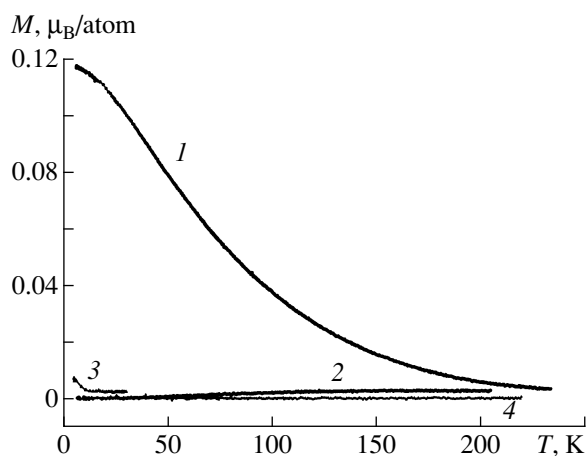
**Fig. 7.11.** ZFC and FC magnetization vs. temperature in the field of 300 Oe for the samples containing 6 wt % Fe–Co (5 : 1) (curve *1*--FC, *2*--ZFC) and 10 wt % Fe–Co (1 : 1) (curve *3*--FC, curve *4*--ZFC); and in the PE matrix (*1*, *3*) FC and (*2*, *4*) ZFC.

The sample with 6 wt % Fe–Co (5 : 1) was prepared by the thermodestruction of the $FeCo(CO)_4$ cluster at 270°C. Its room-temperature $M(H)$ curve (Fig. 7.12) did not demonstrate hysteresis. The temperature ZFC–FC hysteresis appeared below about 250 K, which can be regarded as the blocking temperature for this sample. The low-temperature $M(H)$ curves of this sample are characterized by a strong dependence on its magnetic history. The magnetization curve $M(H)$ measured at 77 K after cooling in a zero magnetic field is located below the room-temperature curve for the fields higher than 300 Oe (Fig. 7.12). A decrease in the magnetization on cooling was observed for the ZFC $M(H)$ curve (Fig. 7.11). At the same time, the FC $M(H)$ curve shows a rapid magnetization increase in the temperature range
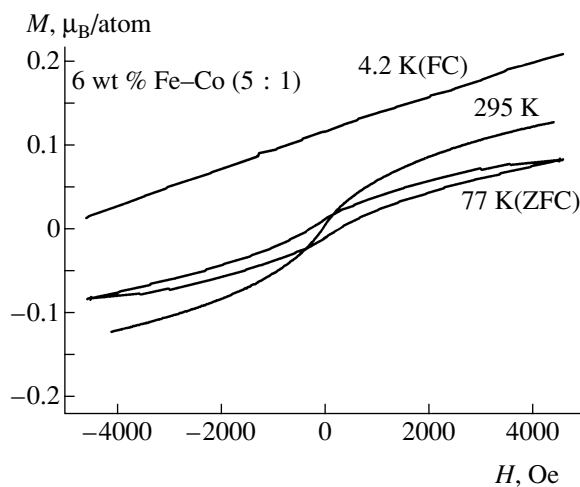
below about 100 K. The demagnetization curve measured at 4.2 K after cooling in a field of 4.5 kOe showed that this field was not sufficient to bring the sample into the demagnetized state. These effects can be associated with the appearance of a noncollinear magnetic structure in the particles on cooling and with the presence of essential exchange anisotropy in a low-temperature region.

The sample containing 6.5 wt % Fe–Sm (3 : 1) was obtained by the thermodestruction of the $FeSm(CO)_n$ cluster at 270°C. Iron-rich Sm–Fe bulk compounds (such as $SmFe_7$, $Sm_2Fe_{17}C_y$) have high magnetic anisotropy and magnetization at room temperature. The $SmFe_7$ anisotropy exceeds that of the well-known permanent magnet NdFeB. These properties become stronger upon the addition of carbon due to the increase in the Curie temperature. Upon the formation of nanoparticles in a polymeric matrix, carbon can transfer from the matrix to the particle with the corresponding effect on magnetic properties. Adding Sm to Fe can also enhance its oxidation resistivity.

Figure 7.13 shows the room-temperature magnetization curve of the Fe–Sm sample. The sample is characterized by a relatively high magnetization (about 1 $\mu_B$/magnetic atom), but the magnetic field hysteresis in the $M(H)$ curve is absent.

### 7.4. Oxide-Based Samples and the $CoCl_2$ Sample

The magnetic properties of various iron oxide nanoparticles have been addressed in many works. Among recent works focusing on $\gamma$-$Fe_2O_3$ nanoparticles, one can note [24, 72–79].

Zhang *et al.* [75] prepared 4–5-nm $\gamma$-$Fe_2O_3$ particles encapsulated within a $SiO_2$ shell by coprecipitation of ferrous and ferric salts. The system of such particles



**Fig. 7.12.** Magnetization curves for the sample containing 6 wt % Fe–Co (5 : 1) in the PE matrix at temperatures of 4.2, 77, and 295 K.
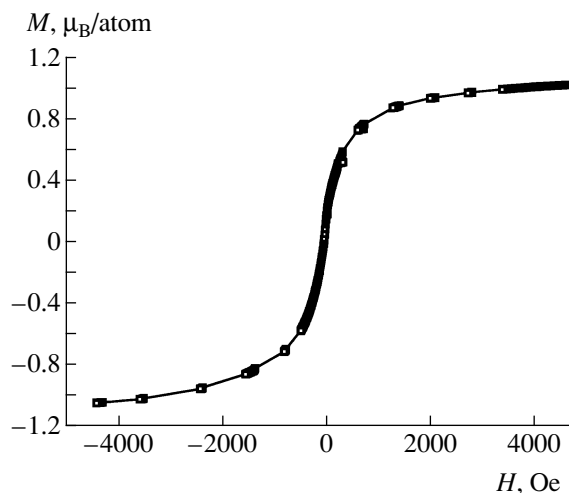


**Fig. 7.13.** Room-temperature magnetization curve of the sample containing 6.5 wt % Fe–Sm (3 : 1) in the PE matrix (magnetization is given per magnetic atom).

exhibited a superparamagnetic behavior in the range from room temperature to the blocking temperature of 15 K. The effective anisotropy constant was estimated from $T_{b}^{m}$ to be $1.57 \times 10^6$ erg/cm$^3$. The magnetization of the system measured in the field of 30 kOe was 20 emu/g Fe$_2$O$_3$ at 5 K and 5 emu/g Fe$_2$O$_3$ at 300 K. Martinez *et al.* [24] fabricated γ-Fe$_2$O$_3$ nanoparticles through a vaporization–condensation process. The resulting powder contained nanoparticles with a mean diameter of about 9–10 nm. The blocking temperature determined from ZFC–FC measurements was about 72 K. An additional anomaly was observed in the FC $M(T)$ curve in the region of 42 K, which was attributed by the authors to the onset of the spin-glass state in the particle surface layer with a thickness of 0.6 nm. The saturation magnetization of the particles was found to be 5 emu/g at 5 K. In the temperature range below about 23 K, the shifted hysteresis loops were observed after field cooling with the exchange shift field of 1500 Oe at 4.2 K. Morales *et al.* [72] obtained γ-Fe$_2$O$_3$ nanoparticles by coprecipitation from solution and by laser pyrolysis of Fe(CO)$_5$. The particles with a mean diameter of 12 nm were characterized by $H_c$ = 29 Oe and $M_s$ = 65.4 emu/g at room temperature (260 Oe and 72.7 emu/g, respectively, at 5 K). For smaller particles, $M_s$ decreased and $H_c$ at 5 K increased (at room temperature, $H_c$ = 0); for 3.5-nm particles, $H_c$ at 5 K was 3 kOe and $M_s$ was 9.9 emu/g. Dormann *et al.* [73] studied the effects of interaction between γ-Fe$_2$O$_3$ nanoparticles dispersed in poly(vinyl alcohol) and in powder.

In [74, 76–79], the systems of γ-Fe$_2$O$_3$ nanoparticles were studied in various matrices. Sohn *et al.* [74] investigated a thin (800 μm) magnetic film containing γ-Fe$_2$O$_3$ particles (5 wt % Fe) with a mean diameter of 5 nm in the [NORCOOH]$_{30}$[MTD]$_{300}$ diblock copolymer (NORCOOH = 2-norbornene-5,6-dicarboxylic acid, MTD = methyltetracyclododecene). The blocking temperature of such a system, determined as the temperature at which the magnetic field hysteresis disappeared, was 16 K. The effective anisotropy constant of the particle system calculated from the $T_{b}^{m}$ value was $1.58 \times 10^6$ erg/cm$^3$. The saturation magnetization of the material was 39 emu/g Fe$_2$O$_3$. The temperature dependence of the coercive force obeyed the $T^{1/2}$ law with $H_c$ = 530 Oe at 0 K. Beutivegna *et al.* [76] prepared the samples containing 0.28 vol % γ-Fe$_2$O$_3$ particles with a mean diameter of 10 nm in a silica xerogel matrix. The saturation magnetization of the nanoparticle system was 24% lower than that of the bulk material, and the anisotropy constant was $1.8 \times 10^5$ erg/cm$^3$. Sappey *et al.* [77] studied a diluted system (the volume concentration of the magnetic component was 0.02%) of γ-Fe$_2$O$_3$ nanoparticles (mean diameter of 7 nm) embedded in the silica matrix. From the ZFC and FC magnetization curves, it was established that the blocking temperature was about 60 K, the coercive force at 0 K
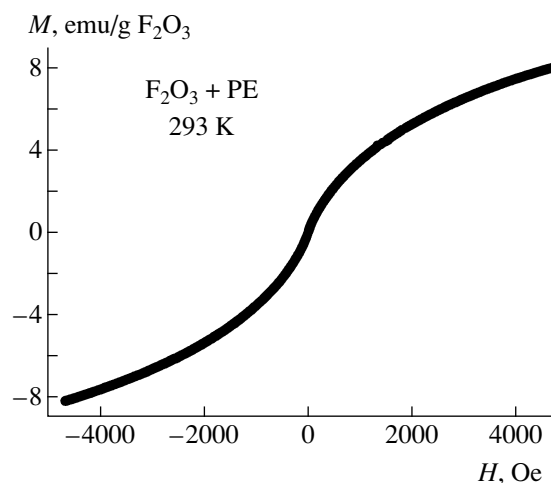


**Fig. 7.14.** Room-temperature magnetization curve of the sample containing 23 wt % Fe$_2$O$_3$ in the PE matrix.

was 250 Oe, and the anisotropy constant was $6.4 \times 10^5$ erg/cm$^3$. The observed anomalous ZFC $M(T)$ peak dependence on magnetic field was explained by the size distribution of the particles. Ziolo *et al.* [78] investigated a material containing γ-Fe$_2$O$_3$ particles with a diameter of 5–10 nm in sulfonated polystyrene. The magnetization of the sample with 21.8 wt % γ-Fe$_2$O$_3$ was almost the same as that of the bulk material. The blocking temperature determined from the magnetization measurements of an analogous sample with 2 wt % γ-Fe$_2$O$_3$ was about 40 K [79]. This material was superparamagnetic at room temperature, and the coercive force of 1200 Oe was observed at 10 K. The magnetization of the sample containing 2 wt % γ-Fe$_2$O$_3$ measured in a field of 9 kOe was three times smaller than that of the bulk γ-Fe$_2$O$_3$.

EXAFS, EPR, and Mössbauer investigations [80] showed that our materials obtained by the thermodestruction of iron acetate Fe$_2$(CH$_3$COO)$_3$ in the polyethylene matrix contained γ-Fe$_2$O$_3$ nanoparticles. The samples with the iron oxide concentration from 1 to 30 wt % were studied. At room temperature, the superparamagnetic behavior was observed. Figure 7.14 shows the $M(H)$ curve for the sample with 23 wt % Fe$_2$O$_3$. The Langevin function (10) fitted to the experimental $M(H)$ curve in Fig. 7.14 gives $M_s$ = 9.6 emu/g Fe$_2$O$_3$ (0.14 μ$_B$/atom) and the average magnetic moment of a particle μ = 4800 μ$_B$. It should be noted that bulk γ-Fe$_2$O$_3$ is a spinel ferrimagnet with a magnetic ordering temperature of 848 K and a saturation magnetization of 81 emu/g at 4.2 K and 76 emu/g at 298 K [44]. The observed saturation magnetization in the nanoparticle system is much lower than that in the bulk material, which is usually related to the emergence of a noncollinear spin structure in the nanosized state stable even in strong magnetic fields [24, 75]. In the samples with a lower γ-Fe$_2$O$_3$ content, the saturation
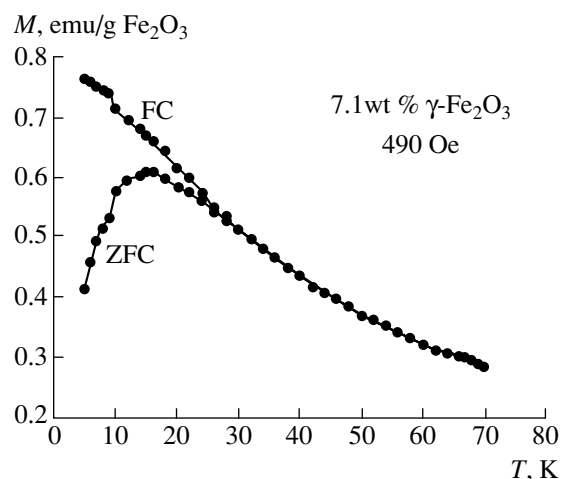
**Fig. 7.15.** ZFC and FC magnetization vs. temperature in the field of 490 Oe for the sample containing 7.1 wt % $\gamma$-$Fe_2O_3$.
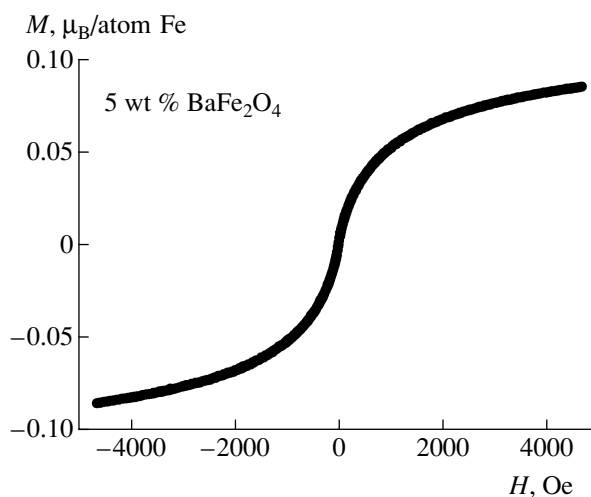


**Fig. 7.16.** Room-temperature magnetization curve for the sample containing 5 wt % $BaFe_2O_4$ in the PE matrix.

magnetization decreased to about 1.5 emu/g for the sample with 1.4 wt % $\gamma$-$Fe_2O_3$. Figure 7.15 shows the ZFC and FC $M(T)$ dependences measured for the sample with 7.1 wt % $\gamma$-$Fe_2O_3$ in the field of 490 Oe. As one can see, there is the temperature ZFC–FC hysteresis below about 30 K. The field hysteresis disappears at 32 K (at 4.2 K, it has a value of 200 Oe). Taking 32 K as the blocking temperature, the effective anisotropy constant $K_{eff}$ was estimated by Eq. (8) (the mean particle diameter was 4 nm) to be $3.2 \times 10^6$ erg/cm$^3$, which is much higher than the bulk value $4.7 \times 10^4$ erg/cm$^3$ [81].

Barium ferrite nanoparticle systems have been studied in [82–86]. Fang *et al.* [82, 83] studied $BaFe_{12-2x}Zn_xSn_xO_{19}$ ($x = 0–1.1$) nanoparticles obtained by chemical coprecipitation. The particle diameter decreased from 95 nm at $x = 0$ to 45 nm at $x = 1.1$. Magnetization measurements were performed for the sam-

ples obtained by the cold pressing of a nanoparticle powder. The approach to the magnetic saturation law was used to determine the saturation magnetization $M_s$ and the anisotropy constant. At low temperatures (78 K), the $M_s(x)$ dependence passes through a maximum, $M_s$ 92 emu/g, at $x = 0.3$. The anisotropy constant at 0 K decreased with an increase in $x$ from $4.1 \times 10^6$ erg/cm$^3$ at $x = 0$ to $2 \times 10^6$ erg/cm$^3$ at $x = 1.1$. The coercive force slightly increased with increasing temperature (at 297 K, it was 1620 Oe at $x = 0.1$ and 5875 Oe at $x = 0$). Ong *et al.* [84] studied magnetic relaxation phenomena in $BaFe_{12-2x}Zn_xSn_xO_{19}$ samples with $x = 0–0.5$. It was shown that with increasing $x$, the magnetic viscosity and fluctuation field increased while the activation volume decreased. These trends were related to a decrease in the particle size, the anisotropy constant, and the wideness of their distribution. The calculated activation volume was much smaller than the actual particle volume, which pointed to the incoherent magnetization reversal mechanism in this system.

Garcia del Muro *et al.* [85] prepared $BaFe_{10.4}Co_{0.8}Ti_{0.8}O_{19}$ particles with different mean diameters (45 and 7.6 nm) by the glass crystallization method. Magnetic measurements were carried out for the samples in which the particles were fixed in the glue matrix in order to prevent their rotation during measurement. The magnetization in the sample with 7.6-nm particles at 5 K was about 58 emu/g in the field of 200 kOe and was not saturated. For 45.4-nm particles, the saturation magnetization at 5 K was 80 emu/g. The coercive force at 5 K was 5500 Oe in the sample with 7.6-nm particles. The ZFC–FC temperature hysteresis was observed below 40 K in the system of 7.6-nm particles even in the field of 70 kOe. The authors attributed the observed magnetic behavior to the spin-glass state in the surface layer of nanoparticles. Liu *et al.* [86] obtained $BaFe_{12}O_{19}$ particles with a mean diameter of 10–30 nm using a complex multistage process involving the formation of hydroxide precursor particles from the water-in-oil microemulsion with subsequently calcining it at temperatures up to 950°C. The powder calcined at 950°C displayed a coercive force of 5639 Oe and a saturation magnetization of 69.74 emu/g at room temperature.

We investigated the samples with 5 wt % $BaOFe_2O_3$, 5 wt % $SrOFe_2O_3$, and 40 wt % $BaFe_2O_4$ and $BaFe_{12}O_{19}$ in the PE matrix. Figure 7.16 shows the $M(H)$ curve for the sample with 5 wt % $BaFe_2O_4$ at room temperature. As one can see, the curve is characterized by the absence of hysteresis and essential curvature. The Langevin function fit gave an $M_s$ value of $0.09 \mu_B$ per Fe atom. ZFC–FC measurements for this sample revealed the blocking behavior (the temperature hysteresis) below about 60 K. This means that the sample displays superparamagnetic properties at room temperature. It should be noted that, according to our EPR measurements, the sample with $BaOFe_2O_3$ mainly consisted of $\gamma$-$Fe_2O_3$, which could explain small values of
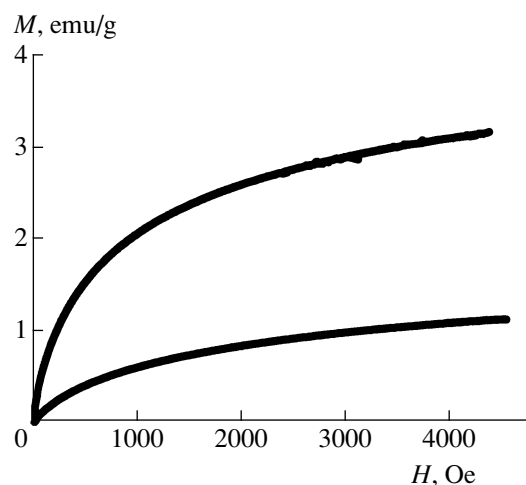
**Fig. 7.17.** Room-temperature magnetization curves for the samples containing 40 wt % $BaFe_2O_4$ and $BaFe_{12}O_{19}$ in the PE matrix (magnetization is given per gram of the magnetic component).



**Fig. 7.18.** FC ($H = 1$ kOe) magnetization (per gram of the magnetic component) vs. temperature for the samples containing 5 wt % Mn in the PE matrix.

magnetization. The increase in the $BaFe_2O_4$ content to 40 wt % did not lead to the appearance of hysteretic properties at room temperature (Fig. 7.17). The field dependence of the magnetization measured for the sample containing 5 wt % $SrOFe_2O_3$ in the PE matrix also did not display hysteresis. The magnetization was rapidly saturated to the value of about 35 emu/g of the magnetic component at 4.5 kOe.

The field dependences of the magnetization $M(H)$ measured at 293 K for the CoO and $CoCl_2$ samples were straight lines with a magnetization of $2.5 \times 10^{-3}$ and $1.4 \times 10^{-2}$ $\mu_B$ per Co atom, respectively. It should be noted that both compounds in the bulk form are antiferromagnetic with Néel temperatures of 292 K for CoO and 25 K for $CoCl_2$ [87, 88].

### 7.5. Manganese-Based Samples

Magnetic molecular clusters with nanometer sizes and high total spins ($S = 10$–14) and, consequently, with large magnetic moments are well known in molecular chemistry. Molecular clusters are the objects with internal magnetic ordering and crystal structure and can be regarded as single-domain nanosized magnetic particles. They are characterized by a well-defined and uniform size and shape, which is important for high-density magnetic recording. The dodecanuclear manganese cluster ("$Mn_{12}$") with the formula $[Mn_{12}O_{12}(CH_3COO)_{16}(H_2O)_4] \cdot 2CH_3COOH \cdot 4H_2O$ has the total spin $S = 10$ with Mn(III) and Mn(IV) spins coupled antiferromagnetically. The high-spin ground state is combined with a strong easy axis anisotropy. The magnetic moment of the cluster $\mu \approx 21$ $\mu_B$ near 40 K [89–91]. The behavior of the cluster in any type of matrix has not hitherto been studied. Preservation of such properties as uniform size and shape, strong easy
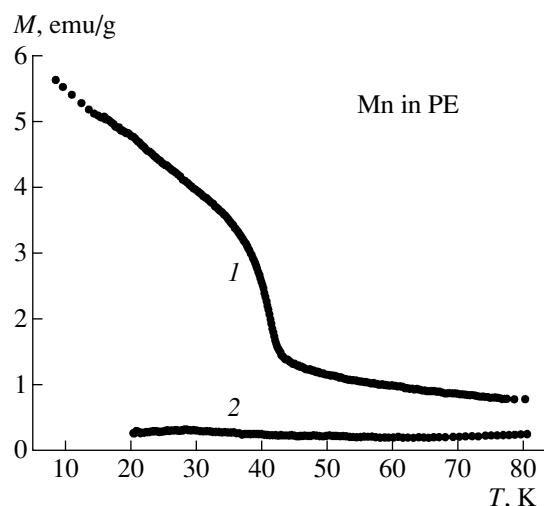
axis anisotropy, and large magnetic moment or, at least, some of these properties in a room-temperature region can give a material with essential advantages for magnetic recording. With this in mind, we decided to make the first step toward the incorporation of molecular clusters into a polymeric matrix.

Figure 7.18 shows the temperature dependences of the FC (1 kOe) magnetization for the samples containing 5 wt % of highly oxidized Mn in the PE matrix. The samples were prepared in order to obtain $Mn_{12}$ in the polyethylene matrix: sample *1* was fabricated using $Mn(CH_3COO)_2$ and $KMnO_4$, and for sample *2*, $H_2O_2$ was used instead of $KMnO_4$. As one can see, magnetization of sample *1* is much higher than that of sample *2*. In the temperature range below 40 K, the magnetization in
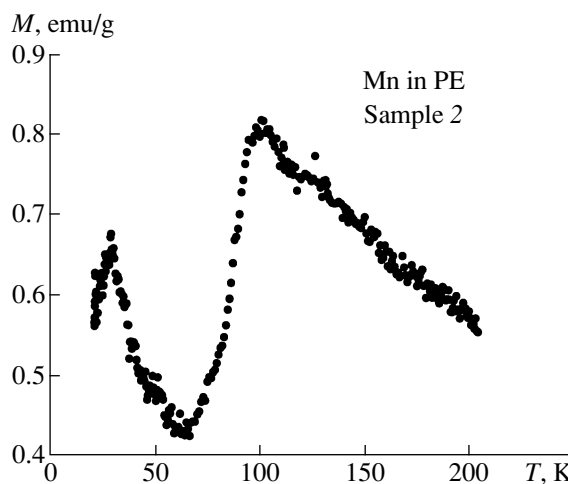


**Fig. 7.19.** FC ($H = 2$ kOe) magnetization (per gram of the magnetic component) vs. temperature for sample *2* containing 5 wt % Mn in the PE matrix.
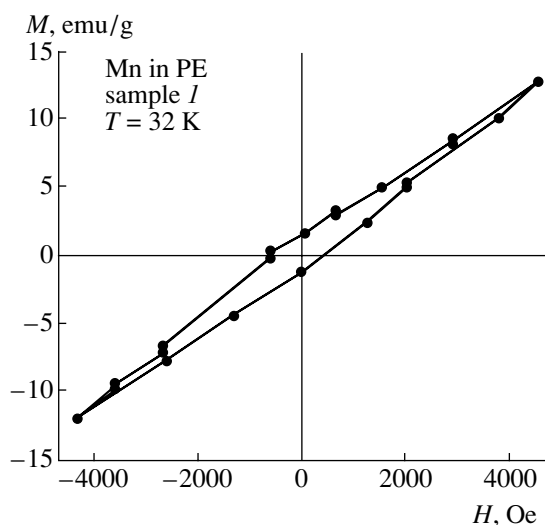
**Fig. 7.20.** Hysteresis loop of sample *1* containing 5 wt % Mn in the PE matrix measured at 32 K.
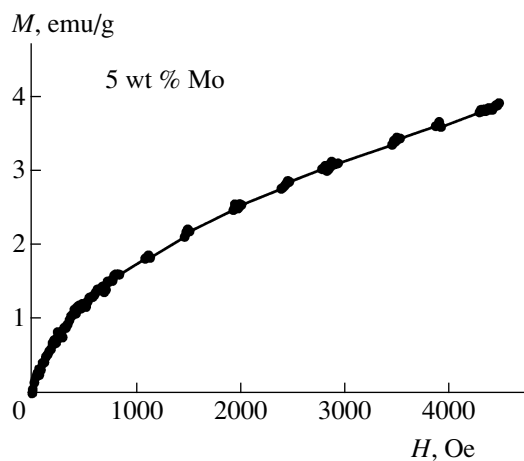


**Fig. 7.21.** Room-temperature magnetization curve of the sample containing 5 wt % Mo in the PE matrix.

sample *1* rapidly increases. Figure 7.19 shows the $M(T)$ of sample *2* measured in the field of 2 kOe on a scale convenient for observation specific features of the curve. As one can see, there are two maxima near 100 K and 40 K. It is known that Mn and its oxide are antiferromagnets with the Neel temperature of 100 and 122 K, respectively [44]. The first maximum (at 100 K) in Fig. 7.19 can be due to antiferromagnetic ordering in Mn and its oxide. The second maximum is observed at about 40 K at which the sharp magnetization increase in sample *1* is observed. It should be noted that the $M(T)$ curve of sample *1* (Fig. 7.18) has a ferromagnetic character (a monotonic increase with decreasing temperature). According to Sessoli *et al.* [90], magnetization ordering in $Mn_{12}$ clusters begins at a temperature of 40 K. The $Mn_{12}$ cluster has a complex magnetic structure formed as a result of the competition between ferro- and antiferromagnetic interactions. It is possible

that the magnetic structure of highly oxidized Mn particles in the sample *1* forms in an analogous way.

Figure 7.20 shows the hysteresis loop measured for sample *1* at a temperature of 32 K. The magnetization curve is not saturated in the field of 4.5 kOe. There is also a coercive force of about 600 Oe, which can be related to the magnetic anisotropy arising from the interaction of the particles with the polyethylene matrix. In the field of 4.5 kOe at 4.2 K, sample *1* had a magnetization of about 0.16 $\mu_B$ per Mn atom. Such a small magnetic moment of Mn atom (as compared with the $Mn_{12}$ cluster) can be caused by insufficient oxidation of Mn during preparation.

The experimental preparation of Mn nanoparticles is the first step on the road to creation of stable materials containing monodisperse nanoparticles (molecular clusters) with significantly elevated magnetic moments. Such nanoparticles can be characterized by a perfect identity, which is very important and promising for the magnetic storage purposes.

### 7.6. Mo-Based Samples

As it was shown in several theoretical studies, magnetism in reduced dimensionality (surface, films, or small particles) is not a priori restricted to the elements exhibiting magnetic properties in the bulk [92, 93]. A possible enhancement of the local density of states of magnetic electrons ($3d$, $4d$, $5d$) at the Fermi level in the surface layer can lead to fulfillment of the Stoner criterion for ferromagnetism even if it is not valid in the bulk state. In the nanosized state, the surface can play a crucial role in the formation of the total magnetic properties of a system due to the essential relative amount of atoms at the surface.

Measurements for gadolinium showed an increase in the surface Curie temperature by about 60 K compared to the bulk value and a canted surface magnetization [94]. Evidence of surface magnetic ordering at the Rh (100) surface (Rh is not magnetic in the bulk state) was obtained by measuring the linear magnetic dichroism [95]. Taniyama *et al.* [96] measured the magnetization in pure Pd particles with a mean diameter of 5.9 and 7.2 nm prepared by the gas evaporation method. It was established that the nanoparticles exhibit magnetic properties, which can be explained assuming that the particles have a ferromagnetic surface and a nonmagnetic core. At 1.8 K, the magnetization of 5.9-nm nanoparticles in the field of 55 kOe was about 0.75 emu/g.

We carried out magnetization measurements for the samples containing 5 wt % Mo or $MoO_3$ in the PE matrix at room temperature. The sample with $MoO_3$ displayed a paramagnetic behavior with the magnetization 5 emu/g $MoO_3$ (0.09 $\mu_B$/atom Mo). $M(H)$ for the sample with 5 wt % Mo (Fig. 7.21) can be represented as consisting of a ferromagnetic component (a sharp magnetization increase at the initial stage) and a strong paramagnetic component (subsequent increase with
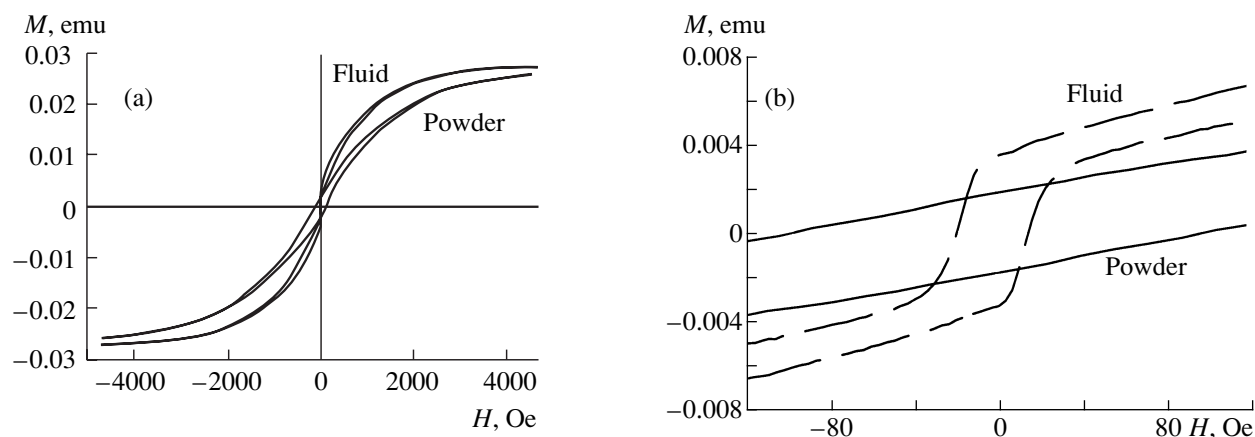
**Fig. 7.22.** Hysteresis loops (in the fields up to (a) 4.5 and (b) 120 Oe) for the samples (fluid and powder) containing NdFeB nanoparticles obtained by electrosparking method.

magnetic field). Similar $M(H)$ curves were observed for Pd nanoparticle systems by Taniyama *et al.* [96] and were accounted for by the ferromagnetic nature of the particle surface layer and the paramagnetic behavior of its core. The magnetization of the Mo sample in 4.5 kOe is about 3.9 emu/g (0.07 $\mu_B$/atom). It should be noted that the magnetic susceptibility in bulk Mo is $9.3 \times 10^{-7}$ emu/g Oe [97], which gives the magnetization value only $4.2 \times 10^{-3}$ emu/g Oe at 4.5 kOe. The observed magnetic properties of the Mo samples point to the possible onset of magnetic ordering and enhancement of paramagnetism in Mo in the nanosized state.

### 7.7. Nd–Fe–B Particles in Styrene

The hysteresis loops of a styrene fluid (suspension) and a powder containing Nd–Fe–B nanoparticles were measured at room temperature (Fig. 7.22a, 7.22b). The samples were obtained by the electrosparking method. The magnetization of the samples at 4.5 kOe was almost the same for the suspension and the powder. At the same time, the coercive force in the latter case was about 9 times higher (100 Oe) than in the case of the suspension. This may be related to the free state of the particles in the suspension or with the more intense interparticle magnetic interactions in the powder due to smaller distances between them. ZFC–FC measurements of the powder did not reveal any peculiarities, which could be related to the blocking temperature. The powder magnetization monotonically increased with temperature up to room temperature. Near 40 K, magnetization increased more sharply, which can be due to the transformation of the internal magnetic structure of the particles.

## 8. CONCLUSIONS

The main aim of this work was to develop novel polymeric materials containing magnetic single-domain nanoparticles suitable for the purposes of high-density magnetic and optical data storage.

To solve this task, the samples containing magnetic nanoparticles with various compositions, including such complex materials as ferrites and heterometallic compounds, in different polymeric matrices were obtained and investigated. For the synthesis of most samples, we used the method of thermodestruction of metal-containing compounds, among which carbonyls, acetates, formates, and complex clusters can be mentioned. The influence of the technological parameters of the synthesis (temperature, stirring speed, existence or absence of the magnetic field, etc.) on the sample properties was studied. A large body of experimental data on variation of the nanoparticle composition, concentration in the samples, nature of matrices, etc., was obtained. It has been shown that the complex of properties and structural parameters of a new material can be changed targetly by controlling the listed parameters.

The samples containing Fe in a wide range of concentrations, Co, Mo, Mn, Fe with Pt, Co, Sm, and Nd; oxides $Fe_2O_3$, $MoO_3$, $CoO$, $BaOFe_2O_3$, $BaFe_{12}O_{19}$, and $SrOFe_2O_3$ were investigated by the X-ray, Mössbauer, EPR, and vibrating sample magnetometer methods. As polymeric matrices, high-pressure polyethylene, syndiotactic and isotactic polypropylene, and polyamide were used. The structure of the nanoparticles in the most promising material containing Fe in the polyethylene matrix was thoroughly investigated and characterized by the Mössbauer, EPR, TEM, SAXS, and other methods. It was shown that the nanoparticles had a complex structure comprising pure Fe and Fe carbides and oxides. Lognormal nanoparticle size distribution was established, the largest particles being no larger than 10 nm in size.

It was established that the polymeric materials containing nanoparticles of Fe, Co, Mn, Pt–Fe, Sm–Fe, Nd–Fe, CoO, BaO–$Fe_2O_3$, $SrOFe_2O_3$, $CoCl_2$, Mo, and $MoO_3$ exhibit a magnetic behavior. Our findings show

that the samples containing Fe or Co in the PE, PP, and PAMD matrices have properties suitable for magnetic recording. The samples with 5 wt % Fe and 4% Co in the PE matrix had especially favorable properties. The first (Fe) sample is characterized by the coercive force in range from 800 to 950 Oe at room temperature and by the blocking temperature of about 400°C. The coercive force of the second (Co) sample is 590 Oe. The room-temperature magnetization in a field of 4.5 kOe for the Fe and Co samples is close to 1.0 $\mu_B$/atom. In the latter case, it can be doubled by heat treatment. The remanent magnetization $M_r$ is about 1/3 of the values in 4.5 kOe. Our magnetization measurements showed the thermal and time stability of the magnetic parameters (coercive force and remanent magnetization) essential for the purposes of data storage for the Fe and Co samples. Mechanical properties of the samples were also quite stable and even higher than in pure polymers.

The coercive force values in our samples are close to those in commercially available floppy and ZIP disks: about 800 Oe for BASF EXTRA 1.44 Mb (the magnetic material is $Fe_2O_3$) and about 1500 Oe for IOMEGA ZIP 100 Mb (the magnetic material is $\alpha$-Fe) (the figures are given in accord with our experimental measurements). Recently, the IBM research center has reported values for the coercive force up to 6 kOe for the film samples prepared from ferrofluids containing FePt nanoparticles obtained by reduction of platinum acetylacetonate by diol and by decomposition of iron pentacarbonyl $Fe(CO)_5$ in high-temperature solution [5]. However, the method used in [5] to fabricate magnetic media is much more complex than ours and at the present stage of development seems not to allow preparation of large quantities of the material.

Our SAXS, TEM, and AFM measurements made for the sample with 5 wt % Fe in the PE matrix gave the value of the nanoparticle diameter of about 3.6 nm. Mössbauer investigations confirmed that the particle diameters did not exceed 10 nm. According to our estimations, the average interparticle distances in the samples containing 5 wt % Fe and 4 wt % Co in the PE matrix should be about 20 nm. In accordance with our calculation, in principle, this could give the value of about 40 Gbit/in$^2$ for the information recording density, assuming that 100 nanoparticles are used for storage of 1 bit of information. The blocking temperature of the Fe sample is at least about 370 K above room temperature, which is a suitable value from the standpoint of storage stability and the power of the existing lasers necessary for optical recording. Both materials containing 4 wt % Co or 5 wt % Fe in the PE matrix can be regarded as very promising for magnetic data recording and storage.

The investigations made in this work also allowed us to obtain new fundamental results, which can be used in further development of magnetic materials for data recording based on polymeric matrices. These results concern the magnetic properties of the samples

obtained by the thermodestruction of MCC (coercive force and magnetization and their temperature dependences, blocking temperature and its concentration dependence), the particle structure and size distribution, and the influence of heat treatment on the magnetic properties of the samples and corresponding transformations inside the particles.

One of first questions arising in relation with the material application as data storage media is which method could be used or adapted to read/write information. As is known, currently available DVD systems use blue solid-state lasers. The future decrease in wavelength is a rather difficult independent task. In principle, the diffraction laws of optics limit information storage density of magneto-optical (MO) media. However, for the writing process in MO media, it is shown that there is no critical problem in creating magnetic domains of smaller size than the Rayleigh resolution limit. On the other hand, the readout process has a critical dependence on the Rayleigh limit, which allows the detection of domains with a minimum size proportional to the wavelength (and numerical aperture). To solve this problem, several readout processes by the magnetically induced superresolution method have been proposed. In these methods, by using the temperature distribution profile from a laser beam and an external magnetic field, it is possible to create a magnetically induced mark region using the polar Kerr effect, rather than read out a recorded mark smaller than the diffraction limit. The realization of these methods needs two or three magnetic layers with an external magnetic field.

In [98], a magnetic superresolution readout process based on a change in the magnetization orientation at high temperature is described. To realize this process, the authors propose a double-layer film composed of a memory layer with perpendicular anisotropy and a readout layer with in-plane magnetization. By heating this film, magnetization in the readout layer rotates from in-plane to perpendicular position by the effect of exchange coupling with the memory layer. This transition occurs in a very short temperature range where the readout process is possible. At other temperatures, the readout-layer magnetization stays in-plane and prevents any domain detection.

It is necessary to note that some other advanced optical methods to read/write information are under development now. One of the ideas in this area is to use near-field optics to minimize the light spot creating bits on the recording media. Near-field optics uses the fact that for short distances from the aperture, light can pass through an aperture much smaller than a wavelength in width. This allows creation of bits smaller than a light wavelength and an increase in recording density. At Lucent Technologies' Bell Laboratories (Murray Hill, NJ), a laser diode with an aperture of 250 nm on its mirrored end was recently developed [99]. With the help of this laser, the Lucent team could write and read optical

data with a density of 7.5 Gb/in$^2$. In future developments, this technology could yield apertures of 30 nm, which could increase data density to more than 500 Gb/in$^2$.

Our experimental results show that the technology created can be considered rather promising for the fabrication of advanced materials for magnetic and optical storage. In our opinion, available samples demonstrate the main properties required for these applications. At the same time, a study to create a commercial prototype of the magnetic storage media should be strongly correlated with activity in creating advanced read/write systems. It should be especially stressed that, as far as we know, the proposed technology is really the first available one that permits the fabrication of kilogram-scale volumes of magnetic materials containing nanoparticles.

## ACKNOWLEDGMENTS

## REFERENCES

1. Gubin, S.P., *Russ. Chem. J.*, 2000, vol. 44, no. 6, p. 23.

2. *Nanomaterials: Synthesis, Properties and Applications*, Edelstein, A.S. and Cammarata, R.C., Eds., Bristol: Institute of Physics Publishing, 1998.

3. Kodama, R.H., *J. Magn. Magn. Mater.*, 1999, vol. 200, p. 359.

4. White, R.L., *J. Magn. Magn. Mater.*, 2000, vol. 209, p. 1.

5. Sun, S., Murray, C.B., Weller, D., Folks, L., and Moser, A., *Science*, 2000, vol. 287, p. 1989.

6. Lohau, J., Moser, A., Rettner, C.T., Best, M.E., and Terris, B.D., *Appl. Phys. Lett.*, 2001, vol. 78, p. 990.

7. Vinogradova, L.M. *et al.*, *Vysokomol. Soedin., Ser. A*, 1970, vol. 12, no. 2, p. 348.

8. Koksharov, Yu.A., Gubin, S.P., Kosobudsky, I.D., Beltran, M., Khodorkovsky, Y., and Tishin, A.M., *J. Appl. Phys.*, 2000, vol. 88, p. 1587.

9. Koksharov, Yu.A., Gubin, S.P., Kosobudsky, I.D., Yurkov, G.Yu., Pankratov, D.A., Ponomarenko, L.A., Mikheev, M.G., Beltran, M., Khodorkovsky, Y., and Tishin, A.M., *Phys. Rev. B: Condens. Matter*, 2000, vol. 63, p. 012407.

10. Koksharov, Yu.A., Pankratov, D.A., Gubin, S.P., Kosobudsky, I.D., Beltran, M., Khodorkovsky, Y., and Tishin, A.M., *J. Appl. Phys.*, 2001, vol. 89, p. 2293.

11. Kliava, J. and Berger, R., *J. Magn. Magn. Mater.*, 1999, vol. 205, p. 328.

12. Raikher, Yu.L. and Stepanov, V.I., *Phys. Rev. B: Condens. Matter*, 1994, vol. 50, p. 6250.

13. Sharma, V.K. and Waldner, F., *J. Appl. Phys.*, 1977, vol. 48, p. 4298.

14. De Biasi, R.S. and Devezas, T.C., *J. Appl. Phys.*, 1977, vol. 49, p. 2466.

15. *Ferromagnetic Resonance*, Vonsovskii, S.V., Ed., Oxford: Pergamon, 1966.

16. Raikher, Yu.L. and Stepanov, V.I., *Phys. Rev. B: Condens. Matter*, 1994, vol. 50, p. 6250.

17. Raikher, Yu.L. and Stepanov, V.I., *J. Magn. Magn. Mater.*, 1995, vol. 149, p. 34.

18. Respaud, M., Goiran, M., Yang, F.H., Broto, J.M., Ould, Ely T., Amiens, C., Chaudret, B., and Askenazy, S., *Physica B*, 1998, vols. 246–247, p. 580.

19. Aharoni, S.M. and Litt, M.H., *J. Appl. Phys.*, 1971, vol. 42, p. 352.

20. Neel, L., *Ann. Geophys. (C.N.R.S.),* 1949, vol. 5, p. 99.

21. Morup, S., Bodker, F., Hendriksen, P.V., and Linderoth, S., *Phys. Rev. B: Condens. Matter*, 1995, vol. 52, p. 287.

22. Leslie-Pelesky, D. and Cowen, J.A., *Phys. Rev. B: Condens. Matter*, 1993, vol. 48, p. 7158.

23. Kodama, R.H. and Berkowitz, A.E., *Phys. Rev. B: Condens. Matter*, 1999, vol. 59, p. 6321.

24. Martínez, B., Obradors, X., Balcells, L., Rouanet, A., and Monty, C., *Phys. Rev. Lett.*, 1998, vol. 80, p. 181.

25. Martínez, B., Roig, A., Molins, E., Gonzalez-Carreno, T., and Serna, C.J., *J. Appl. Phys.*, 1998, vol. 83, p. 3256.

26. Del Bianco, L., Hernando, A., Multigner, M., Prados, C., Sánchez-López, J.C., Fernández, A., Conde, C.F., and Conde, A., *J. Appl. Phys.*, 1998, vol. 84, p. 2189.

27. Nogues, J. and Schuller, I.K., *J. Magn. Magn. Mater.*, 1999, vol. 192, p. 203.

28. Gazeau, F., Bacri, J.C., Gendron, F., Perzynski, R., Raikher, Yu.L., Stepanov, V.I., and Dubois, E., *J. Magn. Magn. Mater.*, 1998, vol. 186, p. 175.

29. Gazeau, F., Shilov, V., Bacri, J.C., Dubois, E., Gendron, F., Perzynski, R., Raikher, Yu.L., and Stepanov, V.I., *J. Magn. Magn. Mater.*, 1999, vol. 202, p. 535.

30. Griffith, J.S., *Mol. Phys.*, 1965, vol. 8, p. 213.

31. Ardelean, I., Peteanu, M., Simon, V., Filip, S., Ciorcas, F., and Todor, I., *J. Magn. Magn. Mater.*, 1999, vols. 196–197, p. 257.

32. Kodama, R.H., Berkowitz, A.E., McNiff, E.J., Jr., and Foner, S., *J. Appl. Phys.*, 1997, vol. 81, p. 5552.

33. Dormann, J., Fiorani, D., and Tronc, E., *J. Magn. Magn. Mater.*, 1999, vol. 202, p. 251.

34. Raikher, Yu.L. and Stepanov, V.I., *Zh. Eksp. Teor. Fiz.*, 1992, vol. 75, p. 764.

35. Smit, J. and Wijn, H.P.J., *Ferrites. Physical Properties of Ferromagnetic Oxides in Relation to Their Technical Applications*, Philip's Technical Library, 1959.

36. Ibrahim, M.M., Edwards, G., Seehra, M.S., Ganguly, B., and Huffman, G.P., *J. Appl. Phys.*, 1995, vol. 75, p. 5873.

37. Chen, C., Kitakami, O., and Shimada, Y., *J. Appl. Phys.*, 1998, vol. 84, p. 2184.

38. Rezlescu, N., Rezlescu, L., Craus, M.L., and Rezlescu, E., *J. Magn. Magn. Mater.*, 1999, vols. 196–197, p. 463.

39. Stoner, E.C. and Wohlfarth, E.P., *Philos. Trans. R. Soc. London, Ser. A*, 1948, vol. 240, p. 599.

GUBIN *et al.*

40. Bean, C.P. and Livingston, J.D., *J. Appl. Phys.*, 1959, vol. 30, p. 120.

41. Jacobs, I.S. and Bean, C.P., *Magnetism*, Rado, G.T. and Suhl, H., Eds., New York: Academic, 1963, vol. 3, p. 271.

42. Chen, C.L., *J. Appl. Phys.*, 1991, vol. 69, p. 5267.

43. Victoria, R.H., *Phys. Rev. Lett.*, 1989, vol. 63, p. 457.

44. Chikazumi, S., *Physics of Magnetism*, New York: Wiley, 1964.

45. Bozorth, R.M., *Ferromagnetism*, New York: IEEE Press, 1993.

46. Hou, D.-L., Nie, X.-F., and Luo, H.-L., *J. Magn. Magn. Mater.*, 1998, vol. 188, pp. 169–172.

47. Bodker, F., Morup, S., Pedersen, M.S., Svedlindh, P., Jonsson, G.T., Garcia-Palacios, J.L., and Lazaro, F.J., *J. Magn. Magn. Mater.,* 1998, vols. 177–181, p. 925.

48. Prados, C., Multigner, M., Hernando, A., Sanchez, J.C., Fernandez, A., Conde, C.F., and Conde, A., *J. Appl. Phys.*, 1999, vol. 85, p. 6118.

49. Santos, A., Ardisson, J.D., Tambourgi, E.B., and Macedo, W.A.A., *J. Magn. Magn. Mater.*, 1998, vols. 171–181, p. 247.

50. Woods, S.I., Kirtley, J.R., Sun, S., and Koch, R.H., *Phys. Rev. Lett.*, 2001, vol. 87, p. 137205-1.

51. Chen, J.P., Sorensen, C.M., Klabunde, K.J., and Hadjipanayis, G.C., *J. Appl. Phys.*, 1994, vol. 76, p. 6316.

52. Respaud, M., Broto, J.M., Rakoto, H., Fert, A.R., Thomas, L., Barbara, B., Verelst, M., Snoeck, E., Lecante, P., Mosset, A., Osuna, J., Ould, Ely T., Amiens, C., and Chaudret, B., *Phys. Rev. B: Condens. Matter*, 1998, vol. 57, p. 2925.

53. Respaud, M., *J. Appl. Phys.*, 1999, vol. 86, p. 556.

54. Peng, D.L., Sumiyama, K., Hihara, T., Yamamuro, S., and Konno, T.J., *Phys. Rev. B: Condens. Matter*, 2000, vol. 61, p. 3103.

55. Gangopadhyay, S., Hadjipanayis, G.C., Sorensen, C.M., and Klabunde, K.J., *J. Appl. Phys.*, 1993, vol. 73, p. 6964.

56. Dupuis, V., Tuaillon, J., Prevel, B., Perez, A., Melinon, P., Guiraud, G., Parent, F., Steren, L.B., Morel, R., Barthelemy, A., Fert, A., Mangin, S., Thomas, L., Wernsdorfer, W., and Barbara, B., *J. Magn. Magn. Mater.*, 1997, vol. 165, p. 42.

57. Jamet, M., Wernsdorfer, W., Thirion, C., Mailly, D., Dupuis, V., Melinon, P., and Perez, A., *Phys. Rev. Lett.*, 2001, vol. 86, p. 4676.

58. Hickey, B.J., Howson, M.A., Greig, D., and Wiser, N., *Phys. Rev. B: Condens. Matter,* 1996, vol. 53, p. 32.

59. Neel, L., *J. Phys. Radium,* 1954, vol. 15, p. 225.

60. Reddy, B.V., Nayak, S.K., Khanna, S.N., Rao, B.K., and Jena, P., *J. Phys. Chem. A.*, 1998, vol. 102, p. 1748.

61. Andriotis, A.N., Lathiotakis, N., and Menon, M., *Chem. Phys. Lett.*, 1996, vol. 260, p. 15.

62. Vega, A., Dorantes-Davila, A., Balbas, L.C., and Pastor, G.M., *Phys. Rev. B: Condens. Matter*, 1993, vol. 47, p. 4742.

63. Billas, I.M.L., Chatelain, A., and de Heer, W.A., *J. Magn. Magn. Mater.*, 1997, vol. 168, p. 64.

64. Billas, I.M.L., Chatelain, A., and de Heer, W.A., *Science,* 1994, vol. 265, p. 1682.

65. Apsel, S.E., Emmert, J.W., Deng, J., and Bloomfield, L.A., *Phys. Rev. Lett.,* 1996, vol. 76, p. 1441.

66. Khanna, S.N. and Linderoth, S., *Phys. Rev. Lett.*, 1991, vol. 67, p. 742.

67. Douglass, D.C., Cox, A.J., Bucher, J.P., and Bloomfield, L.A., *Phys. Rev. B: Condens. Matter*, 1993, vol. 47, p. 12874.

68. Li, X.G., Murai, T., Saito, T., and Takahashi, S., *J. Magn. Magn. Mater.*, 1998, vol. 190, p. 277.

69. Turgut, Z., Nuhfer, N.T., Piehler, H.R., and McHenry, M.E., *J. Appl. Phys.*, 1999, vol. 85, p. 4406.

70. Shinohara, T., Sato, T., Taniyama, T., and Nakatani, I., *J. Magn. Magn. Mater.*, 1999, vols. 196–197, p. 94.

71. Chowdary, K.M., Giri, A.K., Pellerin, K., Majetich, S.A., and Scott, J.H.J., *J. Appl. Phys.*, 1999, vol. 85, p. 4331.

72. Morales, M.P., Andres-Verges, M., Veintemillas-Verdaguer, S., Montero, M.I., and Serna, C.J., *J. Magn. Magn. Mater.*, 1999, vol. 203, p. 146.

73. Dormann, J.L., Fiorani, D., Cherkaoui, R., Tronc, E., Lucari, F., D'Orazio, F., Spinu, L., Nogues, M., Kachkachi, H., and Jolivet, J.P., *J. Magn. Magn. Mater.*, 1999, vol. 203, p. 23.

74. Sohn, B.H., Cohen, R.E., and Papaefthymiou, G.C., *J. Magn. Magn. Mater.*, 1998, vol. 182, p. 216.

75. Zhang, L., Papaefthymiou, G.C., and Ying, J.Y., *J. Appl. Phys.*, 1997, vol. 81, p. 6892.

76. Bentivegna, F., Ferre, J., Nyvlt, M., Jamet, J.P., Imhoff, D.P., Canva, M., Brun, A., Veillet, P., Visnovsky, S., Chaput, F., and Boilot, J.P., *J. Appl. Phys.*, 1998, vol. 83, p. 7776.

77. Sappey, R., Vincent, E., Hadacek, N., Chaput, F., Boilot, J.P., and Zins, D., *Phys. Rev. B: Condens. Matter*, 1997, vol. 56, p. 14551.

78. Ziolo, R.F., Giannelis, E.P., Weinstein, B.A., O'Horo, M.P., Ganguly, B.N., Mehrotra, V., Russell, M.W., and Huffman, D.R., *Science*, 1992, vol. 257, p. 219.

79. Vassiliou, J.K., Mehrotra, V., Russell, M.W., Giannelis, E.P., McMichael, R.D., Shull, R.D., and Ziolo, R.F., *J. Appl. Phys.*, 1993, vol. 73, p. 5109.

80. Yurkov, G.Yu., Gubin, S.P., Pankratov, D.A., Koksharov, Yu.A., Kozinkin, A.V., Spichkin, Yu.I., Nedoseikina, T.I., Pirog, I.V., and Vlasenko, V.G., *Neorg. Mater.*, 2002, vol. 38, no. 2, p. 186.

81. Takei, H. and Chiba, S., *J. Phys. Soc. Jpn.*, 1966, vol. 21, p. 1255.

82. Fang, H.C., Yang, Z., Ong, C.K., Li, Y., and Wang, C.S., *J. Magn. Magn. Mater.*, 1998, vol. 187, p. 129.

83. Fang, H.C., Ong, C.K., Zhang, X.Y., Li, Y., Wang, C.S., and Yang, Z., *J. Magn. Magn. Mater.*, 1999, vol. 191, p. 277.

84. Ong, C.K., Fang, H.C., Yang, Z., and Li, Y., *J. Magn. Magn. Mater.*, 2000, vol. 213, p. 413.

85. Garcia del Muro, M., Batlle, X., and Labarta, A., *J. Magn. Magn. Mater.*, 1999, vols. 196–197, p. 138.

86. Liu, X., Wang, J., Gan, L.M., Ng, S.C., and Ding, J., *J. Magn. Magn. Mater.*, 1998, vol. 184, p. 344.

87. *Fizicheskie velichiny. Spravochnik* (Physical Quantities: A Handbook), Grigor'ev, I.S. and Meilikhov, E.Z., Eds., Moscow: Energoatomizdat, 1991.

88. Carlin, R.L., *Magnetochemistry*, Berlin: Springer, 1986.

89. Caneschi, A., Gatteschi, D., and Sessoli, R., *J. Am. Chem. Soc.*, 1991, vol. 113, p. 5873.

90. Sessoli, R., Tsai, H.L., Schake, A.R., Wang, S., Vincent, J.B., Folting, K., Gatteschi, D., Christou, G., and Hendrickson, D.N., *J. Am. Chem. Soc.*, 1993, vol. 115, p. 1804.

91. Hennion, M., Pardi, L., Mirebeau, I., Suard, E., Sessoli, R., and Caneschi, A., *Phys. Rev. B: Condens. Matter*, 1997, vol. 56, p. 8819.

92. Blügel, S., *Phys. Rev. B: Condens. Matter,* 1995, vol. 51, p. 2025.

93. Taniyama, T., Sato, T., Ohta, E., and Takeda, M., *Physica B*, 1995, vols. 213–214, p. 254.

94. Dowben, P.A., McIlroy, D.N., and Li, D., Surface Magnetism of the Lanthanides, in *Handbook of the Physics and Chemistry of Rare Earths*, 1997, vol. 24, p. 1.

95. Goldoni, A., Baraldi, A., Comelli, G., Lizzit, S., and Paolucci, G., *Phys. Rev. Lett.*, 1999, vol. 82, p. 3156.

96. Taniyama, T., Ohta, E., and Sato, T., *Physica B*, 1997, vols. 237–238, p. 286.

97. Galoshina, E.V., *Usp. Fiz. Nauk*, 1974, vol. 113, p. 105.

98. Sbiaa, R., Le Gall, H., and Yurchenko, S., *J. Magn. Magn. Mater.*, 1999, vol. 195, p. 520.

99. Partovi, A., Peale, D., Wuttig, M., Murray, C.A., Zydzik, G., Hopkins, L., Baldwin, K., Hobson, W.S., Wynn, J., Lopata, J., Dhar, L., Chichester, R., and Yeh, J.H.-J., *Appl. Phys. Lett.*, 1999, vol. 75, p. 1515.